The Australia Telescope 20 GHz Survey: the source catalogue

Tara Murphy,[1,2]★ Elaine M. Sadler,[1] Ronald D. Ekers,[3] Marcella Massardi,[4]
Paul J. Hancock,[1] Elizabeth Mahony,[1,3] Roberto Ricci,[5] Sarah Burke-Spolaor,[3,6]
Mark Calabretta,[3] Rajan Chhetri,[3,7] Gianfranco De Zotti,[4,8] Philip G. Edwards,[3]
Jennifer A. Ekers,[3] Carole A. Jackson,[3] Michael J. Kesteven,[3] Emma Lindley,[1]
Katherine Newton-McGee,[1,3] Chris Phillips,[3] Paul Roberts,[3] Robert J. Sault,[9]
Lister Staveley-Smith,[10] Ravi Subrahmanyan,[11] Mark A. Walker[12]
and Warwick E. Wilson[3]

[1]*Sydney Institute for Astronomy, School of Physics, The University of Sydney, NSW 2006, Australia*
[2]*School of Information Technologies, The University of Sydney, NSW 2006, Australia*
[3]*Australia Telescope National Facility, CSIRO, PO Box 76, Epping, NSW 1710, Australia*
[4]*INAF, Osservatorio Astronomico di Padova, Vicolo dell'Osservatorio 5, I-35122 Padova, Italy*
[5]*Department of Physics and Astronomy, University of Calgary, 2500 University Drive NW Calgary, AB, Canada*
[6]*Swinburne University of Technology, PO Box 218, Hawthorn, Vic 3122, Australia*
[7]*School of Physics, The University of New South Wales, NSW 2052, Australia*
[8]*SISSA/ISAS, Via Beirut 2–4, I-34014 Trieste, Italy*
[9]*School of Physics, The University of Melbourne, Victoria 3010, Australia*
[10]*School of Physics, The University of Western Australia, 35 Stirling Highway Crawley, WA 6009, Australia*
[11]*Raman Research Institute, Sadashivanagar, Bangalore 560080, India*
[12]*Manly Astrophysics, 3/22 Cliff St, Manly 2095, Australia*

ABSTRACT

We present the full source catalogue from the Australia Telescope 20 GHz (AT20G) Survey. The AT20G is a blind radio survey carried out at 20 GHz with the Australia Telescope Compact Array (ATCA) from 2004 to 2008, and covers the whole sky south of declination $0°$. The AT20G source catalogue presented here is an order of magnitude larger than any previous catalogue of high-frequency radio sources, and includes 5890 sources above a 20 GHz flux-density limit of 40 mJy. All AT20G sources have total intensity and polarization measured at 20 GHz, and most sources south of declination $-15°$ also have near-simultaneous flux-density measurements at 5 and 8 GHz. A total of 1559 sources were detected in polarized total intensity at one or more of the three frequencies.

The completeness of the AT20G source catalogue is 91 per cent above 100 mJy beam^{-1} and 79 per cent above 50 mJy beam^{-1} in regions south of declination $-15°$. North of $-15°$, some observations of sources between 14 and 20 h in right ascension were lost due to bad weather and could not be repeated, so the catalogue completeness is lower in this region. Each detected source was visually inspected as part of our quality control process, and so the reliability of the final catalogue is essentially 100 per cent.

We detect a small but significant population of non-thermal sources that are either undetected or have only weak detections in low-frequency catalogues. We introduce the term Ultra-Inverted Spectrum to describe these radio sources, which have a spectral index $\alpha(5, 20) > +0.7$ and which constitute roughly 1.2 per cent of the AT20G sample.

★E-mail: tara@physics.usyd.edu.au

The 20 GHz flux densities measured for the strongest AT20G sources are in excellent agreement with the *Wilkinson Microwave Anisotropy Probe* (*WMAP*) 5-year source catalogue of Wright et al., and we find that the *WMAP* source catalogue is close to complete for sources stronger than 1.5 Jy at 23 GHz.

Key words: methods: data analysis – catalogues – surveys – galaxies: active – cosmic microwave background – radio continuum: general.

1 INTRODUCTION

Large-area high-frequency radio surveys are time-consuming and as a result relatively few large-scale surveys have been carried out. Those that have been completed are either deep but covering small areas, or shallow all-sky surveys. As a result, our knowledge of the high-frequency (>10 GHz) radio-source population is poor.

In addition to the scientific benefits of studying the radio source population at high frequencies, large-scale surveys are useful for foreground subtraction for cosmic microwave background (CMB) experiments. Measurement of CMB anisotropies is limited by contamination from astronomical foregrounds, both Galactic and extragalactic. To improve the efficiency of the component separation techniques, observations such as those of European Space Agency's *Planck* mission are performed on a broad spectral region ranging from a few tenths to hundreds of GHz. At frequencies up to ~100 GHz, extragalactic radio sources are the major contaminants on angular scales smaller than 30 arcmin (de Zotti et al. 2005), so identification of radio sources at high frequencies is critical.

The first blind radio survey above 8 GHz was carried out by Taylor et al. (2001) with the Ryle telescope at 15.2 GHz. The survey covered a 63 deg^2 region and detected 66 sources to a limiting flux density of 20 mJy. Waldram et al. (2003) extended the survey to 520 deg^2, detecting 465 sources to a flux density limit of 25 mJy (the 9C survey). Both surveys found that the existence and flux density of sources at 15 GHz cannot be accurately predicted by extrapolation from lower frequency radio surveys such as the NRAO (National Radio Astronomy Observatory) VLA (Very Large Array) Sky Survey (NVSS) at 1.4 GHz (Condon et al. 1998), further demonstrating the need for large-scale high-frequency surveys for population characterization and source subtraction in CMB studies.

The *Wilkinson Microwave Anisotropy Probe* (*WMAP*) survey, which covers the whole sky at 23, 33, 41, 61 and 94 GHz (Bennett et al. 2003), is the first all-sky radio survey above 5 GHz. The *WMAP* point-source catalogue constructed from the 5-year maps contains 390 sources (Wright et al. 2009), compared to 323 and 208 sources found in the previous 3- and 1-year maps, respectively (Bennett et al. 2003; Hinshaw et al. 2007). Recently, Massardi et al. (2009) have detected 516 sources in the 5-year *WMAP* maps by exploiting a combination of blind and non-blind detection approaches. Section 7 presents a detailed comparison of our AT20G results with the 5-year *WMAP* point-source catalogue.

Table 1 summarizes some earlier large-area high-frequency radio surveys, showing the context in which the AT20G survey was designed. A pilot survey for the AT20G at 18.5 GHz was carried out in 2002 and 2003 with the Australia Telescope Compact Array (ATCA) (Ricci et al. 2004; Sadler et al. 2006) and detected 173 sources stronger than 100 mJy in the declination range −60° to −70°. Ricci et al. (2004) confirmed that the ATCA (with custom hardware) had the capability to rapidly survey the sky at high frequencies. The differential source counts for extragalactic sources

from the pilot survey were found to be in good agreement with the Waldram et al. (2003) 15 GHz survey.

In this paper, we present the full catalogue from the Australia Telescope 20 GHz (AT20G) Survey. The survey covers 20 086 deg^2 (the complete southern sky to declination 0°) to a limiting flux density of 40 mJy beam^{-1}. We followed up candidate sources detected in the survey at 20 GHz and also have near-simultaneous follow-up observations at 5 and 8 GHz for AT20G sources south of declination −15°. An accompanying paper (Massardi et al., in preparation) will provide more detailed statistical analysis of the AT20G sample. A subset of the 320 brightest ($S_{20} > 0.5$ Jy) extragalactic ($|b| > 1°.5$) AT20G sources was presented and discussed by Massardi et al. (2008). The Galactic plane was included in our scanning survey but no follow-up observations were carried out at $|b| < 1°.5$, except for a blind survey of optically thick compact H II regions (Murphy et al. 2009).

In Section 2, we describe the survey and follow-up observations, and in Section 3 we describe the data reduction process. In Section 4, we calculate the accuracy of our measured positions and flux densities. Section 5 presents the source catalogue and defines its format, with the completeness and reliability of the catalogue discussed in Section 6. As an additional investigation into the completeness, Section 7 compares our catalogue with the 5-year *WMAP* results. Finally, Section 8 discusses some statistical properties of the sample and Section 9 presents our conclusions.

2 OBSERVATIONS

The key feature of the AT20G is a two-phase observing strategy. The first phase of our observations exploited the fast scanning capability of the ATCA, using a wideband analogue correlator, to carry out a blind survey. Candidate sources from the scanning survey were then observed in the regular snapshot mode of the ATCA. The results from the scanning survey, which is complete to a deeper level but has lower reliability, will be presented in a companion paper (Hancock et al., in preparation).

2.1 Survey mode

The first phase of our observations consisted of a raster of blind scans of the entire southern sky at 20 GHz, using the ATCA in fast scanning mode (in which it can achieve a speed of 15° min^{-1} in declination at the meridian). The ATCA has low noise very wideband receiver[1] (Moorey et al. 2008) which was used together with a custom analogue correlator. The correlator has 8 GHz bandwidth (Roberts, in preparation) and was originally developed as part of the collaboration for the Taiwanese CMB experiment AMiBA (Lo et al. 2001). We used it to take dual orthogonal polarization data

---

[1] http://www.atnf.csiro.au/projects/mnrf1996/12mm_details.html

Table 1. Comparison of the AT20G with other high-frequency radio surveys. Note that while the *WMAP* images cover the whole sky, regions at low Galactic latitude ($b < 5°$) are excluded from the point-source search. A reanalysis of the *WMAP* survey by Massardi et al. (2009) resulted in a catalogue of 516 sources above a limit of 695 mJy.

Survey	Frequency (GHz)	Sky area (deg^2)	Flux limit (mJy)	*N* sources	Reference/s
Ryle	15	60	20	66	Taylor et al. (2001)
9C	15, 43	520	25	465	Waldram et al. (2003)
9C	15	115	10		Waldram et al. (2009)
9C	15	29	5.5		Waldram et al. (2009)
WMAP	23, 33, 41, 61, 94	32 177	1000	390	Bennett et al. (2003); Hinshaw et al. (2007); Wright et al. (2009)
AT20G pilot	18	1216	100	126	Ricci et al. (2004)
AT20G	5, 8, 20	20 086	40	5867	(This work; Massardi et al. 2008)

Table 2. Observation dates for the scanning observations for each of the declination bands. Overlapping dates are due to patching data being observed at the end of each year's observations.

Declination band	Observation dates
$-30° \geq \delta \geq -40°$	2004 August 11–31
$-40° \geq \delta \geq -50°$	2004 August 20–31
$-50° \geq \delta \geq -60°$	2005 September 9–October 2
$-60° \geq \delta \geq -70°$	2005 September 23–October 2
$-70° \geq \delta \geq -80°$	2005 September 16–20
$-80° \geq \delta \geq -90°$	2005 September 20 and 29
$-15° \geq \delta \geq -30°$	2006 August 16–3
$0° \geq \delta \geq -15°$	2007 August 23–September 9
$-85° \geq \delta \geq -90°$	2007 September 7 and 9

from three of the six 22 m dishes of the ATCA. The lag-correlator measured 16 visibilities as a function of differential delay for each of the three antenna pairs used.

Our custom correlator had no mechanism for allowing for geometrical delay as a function of the position in the sky, so the scans had to be performed along the meridian corresponding to zero delay for the east–west configuration ATCA. All the survey observations used antennas 2, 3 and 4, situated on stations W102, W104 and W106, giving two 30.6 m (2–3 and 3–4) baselines and a single 61.2 m (2–4) baseline. The shortest baseline of 30.6 m means that the survey has reduced sensitivity to extended sources (a 50 per cent reduction in amplitude for source size >45 arcsec). Larger sources will only be included in the survey if they have flux density in smaller angular size cores or hot spots above the survey limit.

The scanning strategy consisted of sweeping sky regions 10° or 15° wide in declination and using the Earth rotation to cover the full 24 h right ascension range in a zigzag pattern. To achieve the Nyquist sky coverage, we used multiple zigzag scanning paths over multiple days – each day the scanning path was shifted by half a beam width. Along with the scan a sample was collected every 54 ms (three samples per beam), which resulted in an rms noise of 12 mJy. Poor-quality scans (due to weather or equipment error) were repeated, so that the sky coverage is as uniform as possible. The analogue correlator outputs for each set of 24 h observations (interleaves) were combined together and calibrated to produce maps with an overall rms noise of $\simeq$10 mJy. Table 2 shows the observing schedule for each declination band in the scanning survey.

The initial calibration of the interleaves was achieved by a daily transit observation of a nearby known calibrator. A second round of calibration was based on those sources from the ATCA calibra-

tor catalogue[2] that fell within each of the interleave observations. Typically there were about 10 such sources within each 24 h observation. A third and final round of calibration was done using newly detected strong sources within the map itself.

The delay steps in the analogue correlator were not precisely equal (as they are in a digital correlator) so the spectrum is not quite the same as the Fourier transform of the lags. Hence, standard synthesis techniques using discrete Fourier transforms could not be used for reliable source detection. Furthermore, the poor (u, v) coverage of the survey (30 and 60 m EW spacings only) required a custom source detection program that worked in a CLEAN-like fashion, detecting the strongest source, fitting a template dirty beam and recording its location and flux estimate before moving to the next source. Sources brighter than 5σ ($\sim$50 mJy beam^{-1}) were scheduled for follow-up observations, as described in the next section.

2.2 Follow-up mode

Each of the candidate sources identified in the first phase of observations was observed in the regular snapshot mode of the ATCA to confirm the detection and to measure an accurate position, flux density and polarization. The flux densities from the initial scan survey are accurate to $\sim$20 per cent (see Hancock et al., in preparation), and so we expected a fraction of the sources to fall below our specified survey detection threshold when re-observed.

The follow-up observations were scheduled to be as close as practical (typically within a few weeks) to the initial survey observations for a particular declination band, to reduce the effects of source variability on survey completeness. Table 3 lists the details of each follow-up run, including the shortest antenna spacing and resolution at each frequency.

The 20 GHz follow-up observations were performed using a hybrid array configuration (i.e. one in which there were north–south as well as east–west baselines) with the standard ATCA digital correlator. We used two 128 MHz bands centred at 18 752 and 21 056 MHz and two polarizations. During data processing, the two bands were combined to form a single 256 MHz wide-band centred at 19 904 MHz which is the reference frequency for our 20 GHz observations.

Candidate sources were prioritized for follow-up observations in the order of decreasing flux density to minimize problems with sample completeness. The sources were scheduled in blocks of $\sim$20 targets, with a nearby secondary calibrator observed for $\sim$5 min at the beginning and end of each block. The sources within each block were observed in the fast mosaicking mode of the ATCA to reduce

[2]http://www.narrabri.atnf.csiro.au/calibrators

Table 3. Follow-up observations at 20 GHz (C), to observe them at 5 and 8 GHz (O) or to repeat previous bad quality observations (R).

Epoch	Declination range	Frequation 1 (MHz)	Frequation 2	Array Config.	Shortest spacing (m)	Beam 1[a] arcsec	Beam 2 arcsec	Dates	Reason
1	$-50°$ to $-30°$	18 752	21 056	H214	80	10.8×10.8		2004 October 21–27	C
1	$-50°$ to $-30°$	4800	8640	1.5C	77	8.3×12.8	4.6×7.13	2004 November 04–08	O
2	$-90°$ to $-50°$	18 752	21 056	H168	61	13.9×13.9		2005 October 27–31	C
2	$-90°$ to $-50°$	4800	8640	1.5C	77	8.3×8.8	4.6×4.9	2005 Nov 12-15	O
3	$-90°$ to $-30°$	18 752	21 056	H214	80	10.8×10.8		2006 April 29–May 03	R
3	$-90°$ to $-30°$	4800	8640	1.5D	107	8.3×9.5	4.6×5.3	2006 June 19–June 23	R,O
4	$-30°$ to $-15°$	18 752	21 056	H214	80	2.0×5.1		2006 October 14–17	C
4	$-30°$ to $-15°$	4800	8640	1.5B	30	8.3×21.1	4.6×11.7	2006 November 9–12	O
5	$-90°$ to $-15°$	18 752	21 056	H214	80	10.8×10.8		2007 May 11–16	R
5	$-90°$ to $-15°$	4800	8640	1.5C	80	8.3×21.1	4.6×11.7	2007 May 4–10	R,O
6	$-90°$ to $0°$	18 752	21 056	H214	80	10.8×10.8		2007 October 26–30	C,R
7	$-15°$ to $0°$	18 752	21 056	H75	31	33.9×33.9		2008 August 22–26	R

[a]Note that the beam size changes with declination, and so these are estimates based on the typical declination of sources observed in a particular epoch.
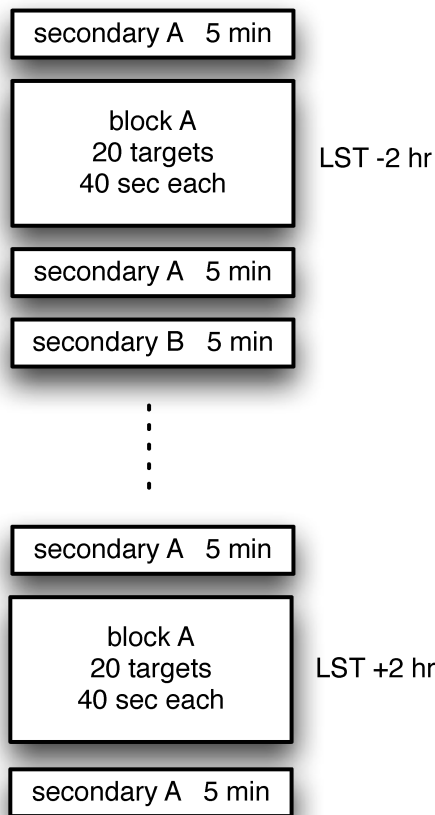
Figure 1. Schematic of the follow-up observing schedule, showing blocks of target sources enclosed by phase calibrators.

the slew time between pointings. We aimed to get two or more 40 s cuts for each source, at different hour angles, so as to obtain reasonable (u, v) plane coverage. Fig. 1 shows a schematic of the observing schedule. Using this method up to 500 candidate sources were observed each day.

For declinations $< -15°$, each 20 GHz observing run was followed by lower frequency observations of the same sets of sources. In these runs, we used an east–west extended array configuration, with two 128 MHz bands centred at 4800 and 8640 MHz. For the rest of this paper, these frequencies will be referred to as '5' and

'8' GHz. The lower frequency observations were conducted within a couple of weeks of the 20 GHz observations, so as to obtain near-simultaneous spectral data for our sample. Sources in the most northern declination band ($\delta > -15°$) were not observed at 5 and 8 GHz because of the poor (u, v) coverage of EW arrays near the equator.

We completed several extra observing runs, at both 20 and 5/8 GHz for the purposes of replacing bad quality data from previous runs. Table 3 lists the details of our observing runs, with the first column showing the matching high frequency–lower frequency epochs. The primary beam full width at half-maximum of the ATCA is 2.4, 5.5 and 9.9 arcmin at 20, 8 and 5 GHz, respectively.

2.3 Additional observations

In addition to the main survey described in this paper, we have completed several complementary sets of observations which will be presented in accompanying papers. In 2006 October, we observed a subsample of the bright sources to obtain high-sensitivity polarization measurements (Burke-Spolaor et al., in preparation). These observations used the most compact configuration of the ATCA (H75), which provides the best coverage of a range of short spacings, and longer integration times than for the main survey, so that higher quality images could be made.

Nine highly extended sources were selected from low-frequency catalogues – the Parkes–MIT–NRAO survey (PMN) at 4.85 GHz (Griffith & Wright 1993) and the Sydney University Molonglo Sky Survey (SUMSS) at 843 MHz (Mauch et al. 2003) – and observed in mosaic mode to improve the flux density estimation at 20 GHz (Burke-Spolaor et al. 2009). Data for seven of these sources have been incorporated into our catalogue in order to avoid flux density underestimation due to resolution effects. However, since we do not have equivalent 5 and 8 GHz observations of these objects we cannot use these data for analyses of radio spectra.

During the AT20G follow-up survey, the 6 km antenna of the ATCA was operational for most of the observing time, however the data from the five much longer baselines could not be easily included in our standard processing pipeline. As a separate programme, we estimated the 6 km visibility by taking the ratio of the scalar amplitude at the 6 km baseline to the scalar amplitude at shorter baselines. This removes the effect of atmospheric decorrelation and avoids the need to phase calibrate the long baselines. Approximately 90 per cent of the AT20G sources have 6 km data available. These 6 km visibilities allow us to identify sources that appear point-like in the

compact configuration, but extended on the 0.3 arcsec scale corresponding to the 6 km baselines. The full analysis and results from this high-resolution follow-up will be presented in Chhetri et al. (in preparation). An immediate application of these data was the identification of extended flat spectrum sources which are either thermal or compact non-thermal sources extended by gravitational lensing. Gravitational lens candidates are being observed with ATCA 6 km configurations at 7 mm. The thermal sources identified by this procedure are Galactic objects, mainly planetary nebulae. They are flagged as Galactic in the main catalogue (see Section 5.4).

2.4 Galactic plane follow-up

Neither the scanning survey nor the follow-up observations were well suited to imaging diffuse Galactic sources. We decided to exclude sources within $|b| < 1°5$ from our main follow-up survey and instead follow up selected subsamples of these sources with targeted observing runs. The first of these was the follow-up of a sample of ultra- and hyper-compact H II regions, selected on the basis of their rising spectral index between 843 MHz (from the Second Epoch Molonglo Galactic Plane Survey; Murphy et al. 2007) and 20 GHz [$\alpha(0.843, 20) > 0.1$]. Further information is given in Murphy et al. (2009).

2.5 Variability sample

Many large-area radio continuum surveys have been conducted at frequencies of 1.4 GHz or below, where the long-term variability of most radio sources is low. As a result, the source catalogues from these surveys can continue to be used with a high level of confidence for many years after the survey was made. This is not necessarily true for surveys at frequencies above 5 GHz, where the source population is increasingly dominated by flat-spectrum radio sources which are expected to be variable (e.g. Condon, Broderick & Seielstad 1989).

To study the variability of the 20 GHz radio source population on time-scales of years, we re-observed a sample of 170 sources (at declination $-60°$ to $-70°$ and with 20 GHz flux densities above 100 mJy) at several epochs over the course of the AT20G survey. All the sources in this variability sample were originally detected in the AT20G Pilot Survey in 2002–2003 (Ricci et al. 2004), giving up to five epochs of observation for some of these sources.

The early (2002–2004) 20 GHz data for the variability sample are discussed by Sadler et al. (2006), who conclude that the general level of variability in sources selected at 20 GHz is relatively low on time-scales of 1–2 years, with a median variability index of 6.9 per cent at 20 GHz over a 1-year time interval. We therefore expect the AT20G catalogue presented here to be reasonably stable, in the sense that if we were to re-observe the survey area on time-scales of a few years we would expect the new source catalogue to contain most of the same sources as the old one.

The AT20G catalogue presented in this paper only lists a single epoch for sources in the variability sample (typically the 2004 observation, except in cases of poor-quality data). A separate paper (Sadler et al., in preparation) will present a full catalogue and detailed analysis of the AT20G variability sample.

3 DATA REDUCTION

We developed a fully automated custom analysis pipeline to edit, calibrate and image the data from the follow-up observations. This included a suite of quality control routines to ensure consistent data quality in the final catalogue. The software was developed using the scripting language PYTHON, and the data reduction was done with the aperture synthesis reduction package MIRIAD (Sault, Teuben & Wright 1995).

The data reduction was followed by a cataloguing stage in which the best quality sources were selected for the final catalogue. This stage also included manual quality control, in which all sources included in the final catalogue were inspected by several AT20G team members (EM, EMS, JAE, RDE, TM). In the rest of this section, we describe the details of the data reduction, quality control and cataloguing. An overview of the process is given in Fig. 2.

3.1 Flagging poor-quality data

Weather conditions can seriously affect the quality of the high-frequency data. Attenuation of the signal by atmospheric water vapour can decrease the sensitivity of the observations, and atmospheric turbulence can produce phase fluctuations that may produce visibility amplitude decorrelation. Hence, data collected in periods of bad weather were removed before further processing. In particular, calibrator data must be of high quality otherwise they introduce errors in the calibration solutions that affect the whole data set.

An atmospheric seeing monitoring system operates at the ATCA site. This measures the differential phase variations in a geostationary satellite signal caused by tropospheric water vapour fluctuations (as described in Middelberg, Sault & Kesteven 2006). We used these data, in conjunction with the system temperature measurements from the antenna receivers (to estimate tropospheric opacity), to develop semi-automatic flagging criteria. Specifically, we discarded data from all the periods in which there was decorrelation greater than 10 per cent. In cases where a calibrator was excluded, the block of target sources associated with that calibrator was also excluded.

In a majority of epochs less than a few per cent of the data were flagged. Very occasionally, bad weather required large blocks of data in the follow-up survey to be edited out. Most of the time we were able to reobserve these blocks in clean-up runs. However, in the declination band $-15°$ to $0°$ there are several regions between 14 and 20 h in right ascension which are still incomplete.

3.2 Calibration

Primary flux calibration and bandpass calibration were done in the standard way using PKS B1934−638, with the assumed fluxes shown in Table 4. More information about the ATCA flux scale at 20 GHz is given in Sault (2003).

For the secondary flux calibration, we followed a non-standard procedure which is summarized in Fig. 3. In each epoch of our observations, we typically observed around ∼50 secondary calibrators. To calculate an accurate flux density for each secondary calibrator, we calculated the mean of the individual snapshot flux densities across the whole run, excluding snapshots which had a flux density greater than two standard deviations away from the mean. Each target source was then calibrated using the secondary calibrator associated with its observing block.

Our observation strategy meant that we had insufficient data to determine the instrumental polarization corrections from the secondary calibrators. Hence, we calculated the leakage terms using the primary calibrator, PKS B1934−638. The linear polarization of this calibrator is known to be not variable and less than 0.2 per cent of the total source flux density at each of our observing frequencies. To determine the leakage terms, it was assumed to be unpolarized.
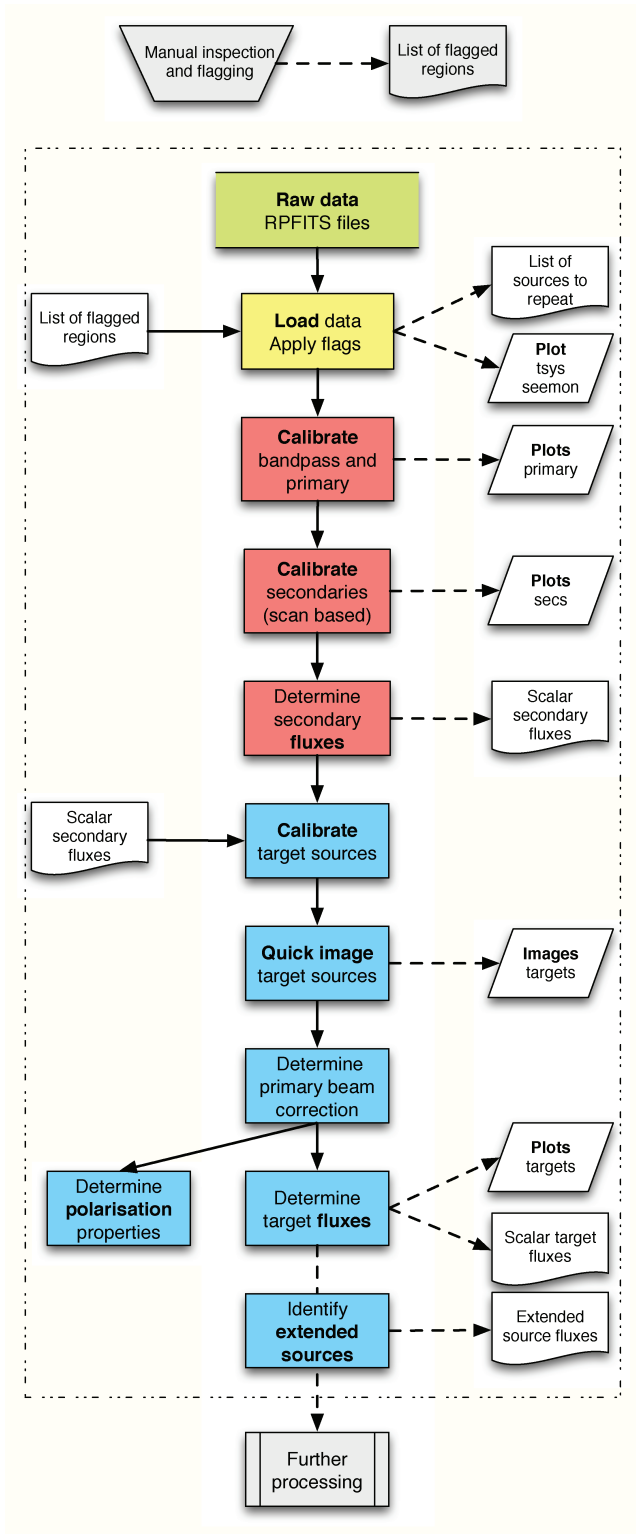
Figure 2. An overview of the AT20G custom data reduction process (see Fig. 3 for more detail about calibration).

Table 4. Assumed fluxes for the primary calibrator PKS B1934−638.

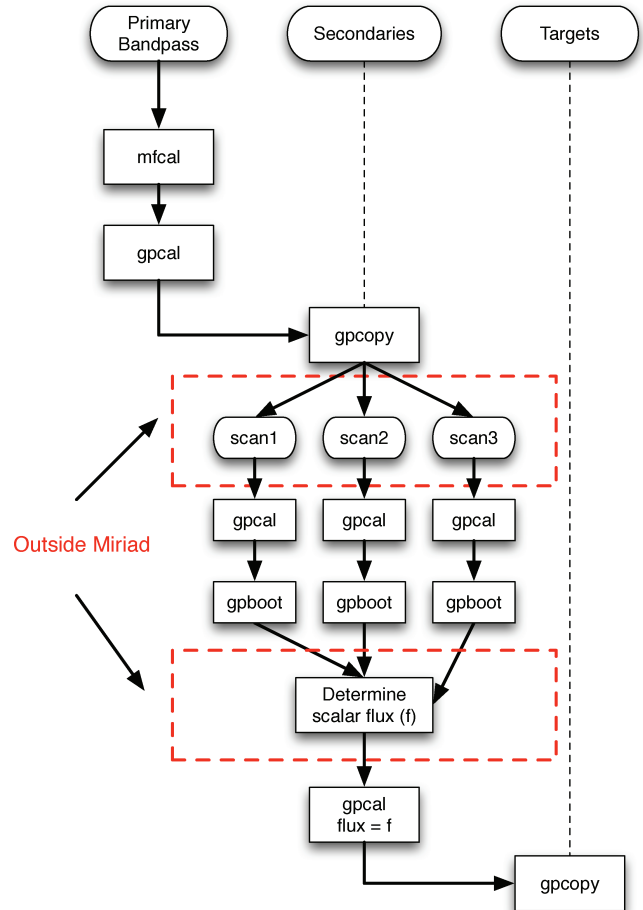| Frequency (MHz)	Flux (Jy)
4800	5.83
8640	2.84
18 752	1.04
21 056	0.88

Figure 3. The custom calibration process developed for the follow-up data reduction.

ibrators. The polarization calibration was then applied to the target sources, and I, Q, U and V Stokes parameters were determined for all of the target sources.

3.3 Flux density measurements

3.3.1 Triple product fluxes

We measured flux densities at all three frequencies using the triple product method implemented in the MIRIAD task CALRED. The amplitude of triple product is the geometric average of the visibility amplitudes in a baseline closure triangle

$$A_{\mathrm{TP}} = \sqrt[3]{A_{1,2} \cdot A_{2,3} \cdot A_{3,1}} \qquad (1)$$

and its phase is the closure phase. Compared to measuring the flux densities from images, as is typical, this method of measuring flux

We adopted these leakage values for all the secondary calibrators, simultaneously calculating the time-dependent complex antenna gains, the residual xy phase differences (x and y are the orthogonal linear polarizations), and the Q and U Stokes parameters of the cal-
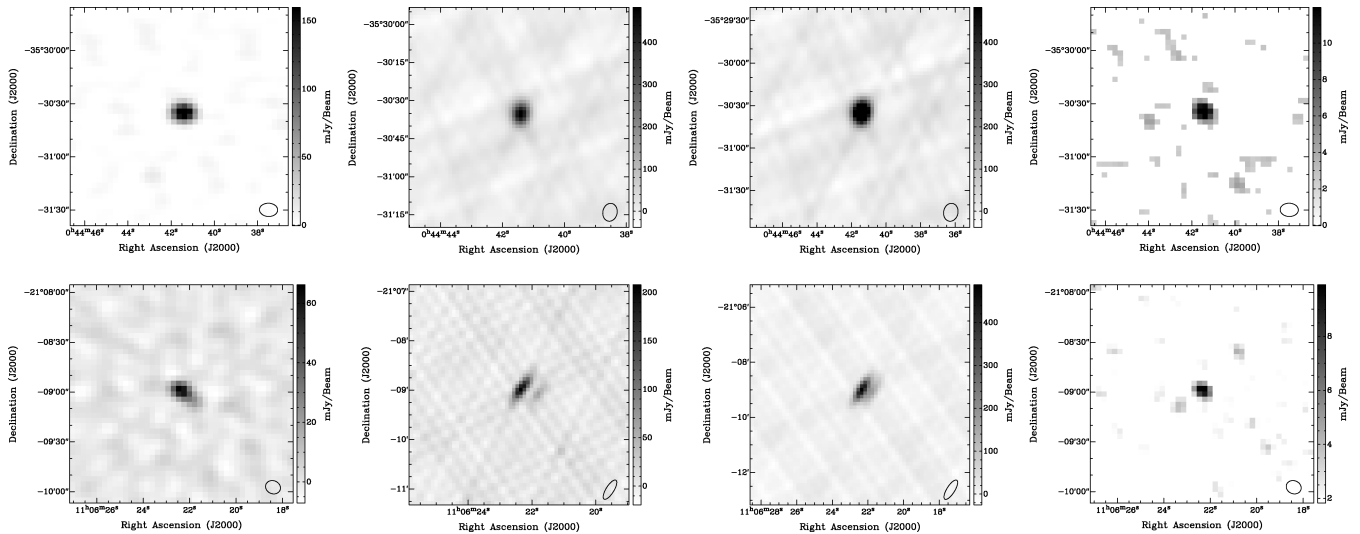
Figure 4. Follow-up images for a typical AT20G point source, J004441−353034 (top panels) and a typical extended source, J110622−210858 (bottom panels). From left- to right-hand panels, they show the total intensity at 20, 8 and 5 GHz, as well as the total polarization map. Note that each image has a different intensity scale.

densities is robust to the effects of phase decorrelation (Ricci et al., in preparation). This meant that we were able to recover flux density measurements for 143 of our target sources that could not be imaged due to poor weather conditions (these are marked as 'poor' in the catalogue).

3.3.2 Extended source fluxes

Sources that are partially resolved, or have multiple components, are not well characterized by the triple product flux measurement. We identified extended sources in our sample using several criteria based on the ratio of the triple product flux density to the flux density measured on the shortest baseline. We visually inspected the 20 GHz visibilities and images for each of these sources to confirm a sample of 337 extended sources. Fig. 4 shows an example of a typical AT20G extended source.

For the extended sources, we calculated the integrated flux densities at 5, 8 and 20 GHz using the amplitude of the signal measured by the shortest baseline. Any source extended at 20 GHz was assumed to be extended at 5 and 8 GHz. In most cases, the shortest physical baseline used in the follow-up observations is either 60 or 80 m (see Table 3), so our 20 GHz flux densities for sources larger than 20 arcsec will still be underestimated using this method. Although improved algorithms could be used, the snapshot observations are inadequate to make reliable estimates. The extended sources will be discussed in more detail in a future paper. Note that the H75 array observations used for epoch 7 have closest spacing of 30 m so the short spacing flux estimate is good for sources up to about 1 arcmin.

For extended sources with multiple components larger than 40 arcsec, the shortest spacing can correspond to a minimum in the visibility and is not a useful estimate of total flux. For these sources, we quote the triple product flux density that would correspond to the flux density of the dominant component and flag the flux as 'poor' in the source catalogue.

Nine of the extremely extended sources were observed separately, and we have used the flux densities determined in Burke-Spolaor et al. (2009) for seven of them. These are discussed in Section 5.1.

3.4 Imaging

We imaged all sources using the standard MIRIAD process, and deconvolved them with a small number of CLEAN iterations (typically 50). This was done primarily for the purpose of visual inspection, since all flux densities were determined using the triple product as discussed in the previous section. Fig. 4 shows examples of a typical point source, AT20G J004441−353034, and a typical extended source, AT20G J110622−210858, at all three frequencies plus the total polarized intensity.

3.5 Polarization

Polarization maps in the four Stokes parameters were created using the MIRIAD routine IMPOL. The total polarized intensity (P) for each source was measured by calculating the fractional polarization (m) in the image at the position of the source, and multiplying it by the flux density calculated using the triple product. The error on the polarized flux was calculated using

$$P_{\mathrm{err}} = \sqrt{2}\frac{\sigma_{\mathrm{n}}}{\chi}, \tag{2}$$

where σ_{n} is the error associated with the noise, which was calculated from the rms noise measured in the Stokes V image, and χ is the ratio of the flux density in the Stokes I image to the flux density as calculated from the triple product. This corrects for phase decorrelation, which would affect both polarized and total flux density in the same way.

The polarized flux was measured at the position of the peak in the Stokes I image. This will be equivalent to the integrated polarization for the unresolved sources but will be neither the peak nor the integrated polarization for the extended sources. For the seven extremely extended sources discussed in Section 5.1, we have used the integrated polarization determined by Burke-Spolaor et al. (2009).

We used the sources observed multiple times as part of the variability sample to investigate the reproducibility of our polarization measurements (see Section 8.1). Based on these experiments we developed the following rules for defining a detection:

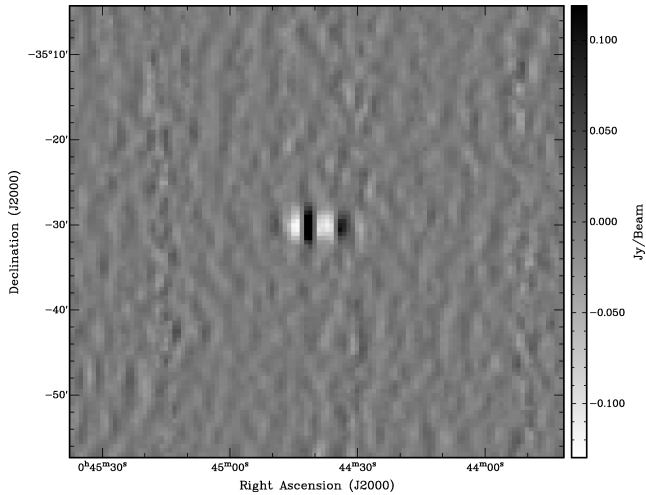(i) if $P \leq 3P_{\mathrm{err}}$, then $P = 3P_{\mathrm{err}}$ as a limit

Figure 5. Image of AT20G J004441−353034 (see Fig. 4), created from the scanning survey data.

(ii) if $m \leq 1$ per cent, then $P = 0.01 S_{20}$ as a limit
(iii) if $P \leq 6$ mJy, then $P = 6$ mJy as a limit,

where P is the total polarized intensity and m is the fractional polarization. If no polarization detection was made, then the limit on the polarized flux density is the maximum of these three limits.

3.6 Cataloguing

All good quality observations were selected for the final source catalogue. In cases where a source was observed in multiple epochs (usually due to there being a poor-quality observation in the earlier epoch), we selected the best source based on the data quality, the presence of near-simultaneous 5/8 GHz data and the offset of the source from the imaging pointing centre. For sources that were observed multiple times as part of the variability study, we selected the first epoch of observation except in cases where that observation was of poor quality.

Due to the poor (u, v) coverage of the scanning survey, a small percentage of the sources scheduled for follow-up observations were in fact sidelobes of the main source. Fig. 5 shows a typical AT20G source as detected in the images created from the scanning survey. The scanning survey has only two different baselines (EW 30 and 60 m) so the images have very high sidelobes. In some cases, bright sidelobes were inadvertently followed up. We excluded sidelobes automatically by grouping all 'duplicate' sources within a radius of 100 arcsec (the effective beam size of the scanning survey) and filtering to keep only the strongest source in the group. Cross-matching with low-frequency surveys also helped to confirm these selections.

All sources were then inspected by several members of the AT20G team, using an online annotation tool. We used this as a final quality control procedure, and to identify any remaining sidelobes. We also used this process to identify extended sources that were not classified by our automatic selection criteria.

4 ACCURACY

4.1 Position uncertainties

The errors in position (σ_α, σ_δ) were calculated using

$$\sigma_\alpha^2 = \sigma_{\alpha,\text{cal}}^2 + \sigma_{\alpha,\text{n}}^2, \tag{3}$$
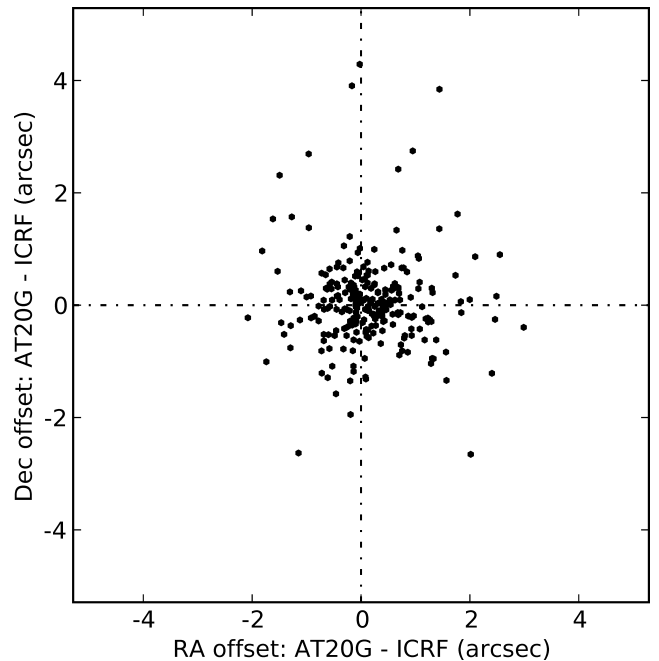

Figure 6. Offset of AT20G 20 GHz positions from ICRF positions for the 251 ICRF calibrators in our catalogue.

$$\sigma_\delta^2 = \sigma_{\delta,\text{cal}}^2 + \sigma_{\delta,\text{n}}^2, \tag{4}$$

where σ_{cal} is the error associated with calibration and σ_{n} is the error associated with the noise.

The calibration term was estimated by comparison with the International Celestial Reference Frame (ICRF) defining calibrators (Fey et al. 2004). The very long baseline interferometry-measured positions in the ICRF catalogue are accurate to a milliarcsecond or below, so any discrepancy between the positions of our target sources and ICRF positions can be assumed to be due to calibration positional errors in our sample. There are 251 ICRF calibrators in our sample, and the positional offsets for these are shown in Fig. 6. The mean offsets in right ascension and declination are $\langle \Delta\alpha \rangle = 0.1$ arcsec and $\langle \Delta\delta \rangle = 0.0$ arcsec, showing that we are in good agreement with the ICRF positions. The values for rms scatter which we used as the calibration terms in equation (3) are $\sigma_{\alpha,\text{cal}} = 0.8$ arcsec and $\sigma_{\delta,\text{cal}} = 0.9$ arcsec.

The calibration term dominates over the noise for our data, so we assumed a common calibration term for all the target sources. From this we calculated the mean positional errors in right ascension and declination for the full sample, giving $\sigma_\alpha = 0.9$ arcsec and $\sigma_\delta = 1.0$ arcsec. Note that this method of calculating positional errors may underestimate the error for extended sources.

4.2 Flux density uncertainties

We calculated the errors in the flux density measurements by adding in quadrature the error associated with calibration (gain error, σ_{gain}) and the error associated with the noise level (σ_{n}):

$$\sigma^2 = \sigma_{\text{gain}}^2 S^2 + \sigma_{\text{n}}^2. \tag{5}$$

The gain error is a multiplicative term (i.e. it is proportional to the source flux density) and is a measure of the gain stability over time. We estimated σ_{gain} for each observational epoch and frequency
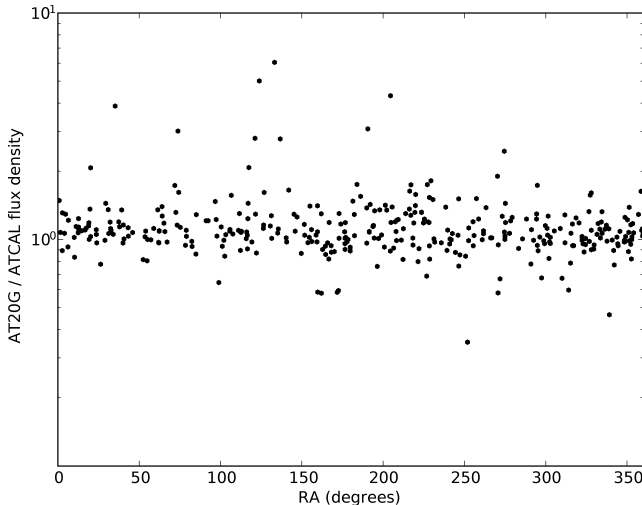
Figure 7. The ratio of AT20G 20 GHz flux density to the Australia Telescope Calibrator Catalogue flux density, for the 362 AT calibrators in our catalogue. The AT calibrator flux density closest in time to our AT20G observations was chosen.

from the scatter in the visibility amplitudes of the calibrators in each observing run. The mean values for the gain errors were found to be of the order of a few per cent. The noise term is an additive term related to the interferometer noise, which is proportional to the system temperature. Since no source has significant flux in Stokes V, the rms noise levels in the V images have no gain error and were used as an estimate of σ_n. The error in the flux density for each source is given in the main catalogue (Table 4). Typically the error is 4–5 per cent of the total flux density.

For extended sources, the error was multiplied by the square root of the number of baselines n_{base} (normally 10 for our five-antenna follow-up arrays) to correct for the fact that the flux densities for these sources are estimated using only one (the shortest) baseline instead of n_{base}.

Many of the sources in the Australia Telescope calibrator catalogue were observed as target sources as part of the AT20G programme. We used these sources to check the integrity of our observing and data reduction procedures. There are 362 AT calibrators in the final AT20G catalogue. For each of these, we extracted the AT calibrator catalogue flux density measurement that was closest in time to our AT20G observations of that source. Fig. 7 shows the AT calibrator catalogue to AT20G flux density ratio for these sources. The median AT20G/AT flux density ratio is 1.06 ± 0.03. All of the outliers were found to be either extended or highly variable sources.

A small number of our target sources are included in the VLA Calibrator Manual.[3] We used these as an additional check on our flux density measurements, particularly for sources near the equator. The VLA calibrator data are only available up to the year 2000. This means that there is a significant difference in the times that these measurements were made. The scatter we see in our sample is quite high, due to variability of the sources over this 8-year period. The median AT20G/VLA flux density ratio for these sources is 1.08 ± 0.10.

We have explored the reasons for the possible flux scale differences between AT20G, and ATCA and VLA calibrators. However, without simultaneous measurements on both telescopes it is dif-

ficult to obtain a conclusive result. We see no evidence that our catalogue flux densities are not on the scale set by the assumed flux of 1934−638. We note that our fluxes are consistent with the *WMAP* flux scale (see Section 7) and strongly recommend a future programme of simultaneous measurements of calibrator sources to tie the flux scales in the North and South hemispheres, and between the major radio observatories.

5 SOURCE CATALOGUE

The primary AT20G source catalogue gives the flux density and polarization measurements at 20, 8 and 5 GHz, as well as the epoch of observation and quality flags. Table 5 shows the first 30 sources in the catalogue; the full catalogue is included in the Supporting Information for this paper, and is available online through Vizier.[4] The columns are:

(1) AT20G source name.
(2–3) Right ascension and declination (J2000). The mean errors ($\sigma_\alpha = 0.9$ arcsec, $\sigma_\delta = 1.0$ arcsec) are derived in Section 4.
(4–5) Flux density at 20 GHz and error in mJy.
(6–7) Flux density at 8 GHz and error in mJy.
(8–9) Flux density at 5 GHz and error in mJy.
(10) Epoch of observation for the three frequencies (20, 8 and 5 GHz).
The epoch codes are listed in Column 1 of Table 3.
(11) Quality flag (see the description below)
(12) Other flags (see the description below)
(13–14) Polarized intensity at 20 GHz and error in mJy.
(15) Fractional polarization at 20 GHz.
(16) Position angle at 20 GHz.
(17–18) Polarized intensity at 8 GHz and error in mJy.
(19) Fractional polarization at 8 GHz.
(20) Position angle at 8 GHz.
(21–22) Polarized intensity at 5 GHz and error in mJy.
(23) Fractional polarization at 5 GHz.
(24) Position angle at 5 GHz.

Column 11 contains a quality flag, either *g* (good, 5501 sources) or *p* (poor, 389 sources). A poor-quality flag indicates that there were lower quality data in that observation, or that, in the case of an extended source, the triple product flux was used rather than the shortest baseline flux. Hence, the flux density measurement for poor-quality sources may not be as reliable.

Column 12 contains other flags identifying the following source types or issues:

e Source is extended and the shortest baseline flux has been used (see Section 3.3).
h Source identified as a Galactic H II region (Section 5.4).
p Source identified as a Galactic Planetary Nebula (Section 5.4).
m Source identified as part of the Magellanic Clouds (Section 5.3).
l Source has no match in the low-frequency surveys (NVSS and SUMSS) (Section 8.4).
b Source is large and extended (see Table 6). The data in the catalogue come from the observations presented in Burke-Spolaor et al. (2009) and discussed in Section 5.1.

AT20G catalogue sources should be referred to by their full IAU designation (Lortet, Borde & Ochsenbein 1994). These are of the

---

[3] http://www.vla.nrao.edu/astro/calib/manual

[4] http://vizier.u-strasbg.fr

Table 5. The first 30 sources in the AT20G source catalogue. The full catalogue is included in the Supporting Information for this paper, and available online through Vizier.[a]

IAU designation	α (J2000)	δ (J2000)	S20 (mJy)	σ_S20 (mJy)	S8 (mJy)	σ_S8 (mJy)	S5 (mJy)	σ_S5 (mJy)	Ep[a]	Q[b]	F[c]	P20 (mJy)	σ_P20 (mJy)	m (per cent)	PA20 (°)	P8 (mJy)	σ_P8 (mJy)	m (per cent)	PA8 (°)	P5 (mJy)	σ_P5 (mJy)	m (per cent)	PA5 (°)
AT20G J000012−853919	00:00:12.78	−85:39:19.9	98	5	63	4	63	4	222	g	·	<10	–	<9.8	–	<6	–	<9.6	–	<6	–	<9.5	–
AT20G J000020−322101	00:00:20.38	−32:21:01.2	118	6	315	16	515	26	111	g	·	<6	–	<5.1	–	<6	–	<1.9	–	<6	–	<1.2	–
AT20G J000105−155107	00:01:05.42	−15:51:07.2	297	19	295	15	257	13	444	g	·	<8	–	<2.7	–	<6	–	<2.0	–	<6	–	<2.3	–
AT20G J000106−174126	00:01:06.31	−17:41:26.2	73	8	–	–	–	–	6···	g	·	<6	–	<8.6	–	–	–	–	–	–	–	–	–
AT20G J000118−074626	00:01:18.04	−07:46:26.8	177	9	–	–	–	–	6···	g	·	<8	–	<4.4	–	–	–	–	–	–	–	–	–
AT20G J000124−043759	00:01:24.50	−04:37:59.6	50	3	–	–	–	–	6···	g	·	<6	–	<12.6	–	–	–	–	–	–	–	–	–
AT20G J000125−065624	00:01:25.59	−06:56:24.7	77	4	–	–	–	–	6···	g	·	<8	–	<10.2	–	–	–	–	–	–	–	–	–
AT20G J000212−215309	00:02:12.02	−21:53:09.9	165	11	–	–	–	–	4···	g	·	<6	–	<3.6	–	–	–	–	–	–	–	–	–
AT20G J000221−140643	00:02:21.71	−14:06:43.9	48	3	–	–	–	–	7···	g	·	<6	–	<12.4	–	–	–	–	–	–	–	–	–
AT20G J000230−033140	00:02:30.60	−03:31:40.1	53	3	–	–	–	–	6···	g	·	<9	–	<17.5	–	–	–	–	–	–	–	–	–
AT20G J000249−211419	00:02:49.85	−21:14:19.2	100	7	–	–	–	–	4···	g	·	<7	–	<6.9	–	–	–	–	–	–	–	–	–
AT20G J000252−594814	00:02:52.93	−59:48:14.0	71	3	64	3	57	3	222	g	·	<9	–	<12.2	–	<6	–	<9.4	–	<6	–	<10.5	–
AT20G J000253−562110	00:02:53.65	−56:21:10.8	94	5	229	12	403	20	222	g	·	<8	–	<8.3	–	<6	–	<2.6	–	<6	–	<1.5	–
AT20G J000303−553007	00:03:03.45	−55:30:07.1	44	3	48	3	52	3	222	g	·	<7	–	<17.0	–	<6	–	<12.6	–	<6	–	<11.5	–
AT20G J000311−544516	00:03:11.04	−54:45:16.8	95	3	313	3	552	9	222	g	e	<8	–	<19.9	–	<6	–	<11.8	–	15	2	8.0	−28
AT20G J000313−590547	00:03:13.33	−59:05:47.7	49	3	101	5	151	8	222	g	·	<8	–	<17.2	–	<6	–	<5.9	–	<6	–	<4.0	–
AT20G J000316−194150	00:03:16.06	−19:41:50.7	76	5	162	9	182	9	444	g	·	<8	–	<10.6	–	<7	–	<4.4	–	<6	–	<3.3	–
AT20G J000322−172711	00:03:22.05	−17:27:11.9	386	43	–	–	–	–	6···	g	·	14	2	3.7	18	<6	–	–	–	<6	–	–	–
AT20G J000327−154705	00:03:27.35	−15:47:05.4	129	8	–	–	–	–	4···	g	·	<10	–	<7.5	–	–	–	–	–	–	–	–	–
AT20G J000404−114858	00:04:04.88	−11:48:58.0	680	32	–	–	–	–	6···	g	·	<7	–	<1.0	–	–	–	–	–	–	–	–	–
AT20G J000407−434510	00:04:07.24	−43:45:10.0	199	10	211	11	244	12	111	g	·	<8	–	<4.1	–	<6	–	<2.8	–	<6	–	<2.5	–
AT20G J000413−525458	00:04:13.97	−52:54:58.7	65	3	98	4	192	6	222	g	e	<7	–	<15.7	–	<6	–	<14.2	–	<6	–	<8.4	–
AT20G J000435−473619	00:04:35.65	−47:36:19.0	868	36	970	49	900	45	111	g	·	15	3	1.7	−51	30	2	3.1	−45	25	1	2.8	−43
AT20G J000505−344549	00:05:05.94	−34:45:49.6	131	6	142	7	134	7	111	g	·	<6	–	<4.6	–	<6	–	<4.2	–	<6	–	<4.5	–
AT20G J000507−013244	00:05:07.03	−01:32:44.6	81	4	–	–	–	–	6···	g	·	<6	–	<7.8	–	–	–	–	–	–	–	–	–
AT20G J000518−164804	00:05:18.01	−16:48:04.9	142	9	–	–	–	–	4···	g	·	<6	–	<4.2	–	–	–	–	–	–	–	–	–
AT20G J000558−562828	00:05:58.32	−56:28:28.9	151	5	376	5	677	11	222	g	e	<7	–	<7.2	–	<6	–	<8.5	–	<6	–	<2.7	–
AT20G J000600−313215	00:06:00.47	−31:32:15.0	63	4	53	3	52	3	111	g	·	<9	–	<13.8	–	<6	–	<11.3	–	<6	–	<11.6	–
AT20G J000601−295549	00:06:01.14	−29:55:49.6	97	6	187	10	228	10	444	g	·	<6	–	<6.2	–	<7	–	<3.9	–	<6	–	<2.6	–
AT20G J000601−423439	00:06:01.95	−42:34:39.8	110	5	259	14	532	27	111	g	·	11	3	9.8	32	14	1	5.5	22	<6	–	<1.1	–

Notes. [a]Epoch of follow-up observations for 20, 8 and 5 GHz fluxes, respectively. The epochs are listed in Table 3.
[b]Quality flag: g (good) or p (poor). [c]Other flags: see Section 5 for the description.
[a]http://vizier.u-strasbg.fr

Table 6. Properties of seven bright extended sources from Burke-Spolaor et al. (2009) that have been included in the AT20G source catalogue. Core and total integrated flux density (or limits) and errors are given in Jy.

AT20G name	Source name	S_{core} (Jy)	S_{18} (Jy)
AT20G J013357−362935	PKS 0131−36	0.03 ± 0.01	>0.44
AT20G J051949−454643	Pictor A	1.32 ± 0.04	6.32 ± 0.11
AT20G J132527−430104	Centaurus A	5.98 ± 0.17	>28.35
AT20G J134649−602430	Centaurus B	5.02 ± 0.06	8.89 ± 0.43
AT20G J161505−605427	PKS 1610−60	0.14 ± 0.05	2.11 ± 0.04
AT20G J215706−694123	PKS 2153−69	–	3.40 ± 0.21
AT20G J235904−605503	PKS 2356−61	0.09 ± 0.03	1.64 ± 0.05

form AT20G *JHHMMSS−DDMMSS*, where AT20G is the survey acronym, *J* specifies J2000.0 coordinate equinox, *HHMMSS* are the hours, minutes and truncated seconds of right ascension, '−' is the sign of declination and *DDMMSS* are the degrees, minutes and truncated seconds of declination.

5.1 Bright extended sources

As discussed in Massardi et al. (2008), a small number of highly extended sources were expected to have a 20 GHz flux density above our bright source sample (BSS) cut-off of 0.5 Jy, but were undetected or had diminished levels of observed emission in the AT20G follow-up observations due to the sources' extent beyond our observing resolution and field of view (∼2.4 arcmin). These sources were identified using extrapolated flux densities from the 5 GHz PMN (Griffith & Wright 1993) and the 0.843 MHz SUMSS (Mauch et al. 2003) data. Integrated flux density and polarization measurements for these sources (shown in Table 6) were measured from mosaic observations done during the 2006 October polarization follow-up run. Their flux densities have been included in our main catalogue and are flagged with a *b*. The observations and data analysis are discussed fully in Burke-Spolaor et al. (2009). The objects with mosaiced measurements are limited to sources south of $\delta = -30°$.

We note that as discussed in Section 2.1, our survey will be incomplete for sources larger than 45 arcsec and based on simple source count arguments many hundred sources larger than a few arcminutes will be missing. Since non-thermal extended sources have steep radio spectra, we suggest that low-frequency catalogues such as NVSS or SUMSS rather than AT20G be used if complete samples of the extended sources are important.

5.2 Comparison with bright source sample

Some bright sources ($S_{20} > 0.5$ Jy) in this catalogue have slightly different parameters than were given in the BSS paper (Massardi et al. 2008). There are 23 sources which have a flux density that differs by more than 10 per cent from the BSS results. In most cases, this is due to a different observational epoch being selected for the source in the BSS than for that in the current catalogue. The largest group of sources in this category is sources from the variability sample discussed in Section 2.5. In the selection of sources for this catalogue, we gave preference where possible to the epoch with simultaneous 5 and 8 GHz observations. However, in the BSS the best quality epoch at 20 GHz was chosen regardless of the availability of follow-up at other frequencies.

5.3 Magellanic clouds

The AT20G survey area includes the Large Magellanic Cloud (LMC) and Small Magellanic Cloud (SMC), and we would expect to find some radio sources in these galaxies, which are effectively foreground sources for cosmological studies. In earlier work using the AT20G pilot survey data, Ricci et al. (2004) and Sadler et al. (2006) simply removed $5° \times 5°$ regions of sky around the LMC and SMC to avoid the problem of foreground contamination. However, since the compact, high-frequency LMC/SMC radio sources are likely to be interesting in their own right, we have now attempted to identify them individually in the final AT20G catalogue.

We searched two areas of sky defined by the following (J2000) coordinates:

SMC $00:30 < \alpha < 01:30$ $-71° < \delta < -75°$

LMC $04:45 < \alpha < 06:00$ $-66° < \delta < -72°$.

There are six AT20G sources in the SMC region and 21 in the LMC region. As with Galactic sources, some LMC and SMC radio sources may have complex, extended emission which is not well imaged by the AT20G snapshot observations. In such cases, the flux densities and positions listed in the AT20G catalogue should be regarded as no more than indicative. Hence, one of the main reasons for identifying LMC/SMC sources is to have the option of excluding them from later analysis of the extragalactic AT20G sample.

To determine whether each 20 GHz source was likely to be associated with the LMC or SMC, we searched the NASA/IPAC Extragalactic Database (NED)[5] for known LMC/SMC objects at or near the AT20G position, and cross-matched the AT20G positions with lower frequency radio catalogues from Filipović et al. (2005) and Payne et al. (2004), who independently classified many of these sources as either LMC/SMC or background objects. We also checked for optical nebulosity of the sources by inspecting overlays of AT20G contours on optical images from the SuperCOSMOS Sky Surveys.

In most cases, it was possible to distinguish foreground LMC/SMC objects from background active galactic nuclei (AGN) with a high level of confidence. We classified 14 of the 27 sources as background extragalactic objects and 13 as LMC/SMC radio sources (listed in Table 7 and identified in the catalogue with a flag '*m*'). As expected most of the LMC/SMC objects are H II regions, but the AT20G catalogue also includes two LMC pulsar wind nebulae, PSR J0537−69 and PSR B0540−69.3.

---

[5] http://nedwww.ipac.caltech.edu

Table 7. AT20G sources which are probably associated with objects in the LMC and SMC.

AT20G name	AT20G position (J2000)	Notes
SMC objects		
J012407−730904	01 24 07.92 −73 09 04.1	IRAS 01228−7324, H II
J012930−733311	01 29 30.07 −73 33 11.3	IRAS 01283−7349, H II
LMC objects		
J045153−692329	04 51 53.25 −69 23 29.4	IRAS 04521−6928, H II
J050950−685305	05 09 50.61 −68 53 05.6	Part of NGC 1858, H II
J051317−692222	05 13 17.75 −69 22 22.6	Large H II region complex
J052212−675832	05 22 12.67 −67 58 32.9	Part of NGC 1936, H II
J053745−691010	05 37 45.51 −69 10 10.0	PSR J0537−69, PWN
J053845−690503	05 38 45.66 −69 05 03.1	Part of NGC 2070, H II
J053937−694526	05 39 37.41 −69 45 26.4	Part of NGC 2079, H II
J053945−693839	05 39 45.57 −69 38 39.2	NGC 2080, H II
J054004−694438	05 40 04.76 −69 44 38.6	Part of NGC 2079, H II
J054011−691953	05 40 11.09 −69 19 53.4	PSR B0540−69.3, PWN
J054024−694014	05 40 24.69 −69 40 14.5	IC 2145, H II
Background sources		
J004047−714559	00 40 47.90 −71 45 59.6	
J005611−710707	00 56 11.34 −71 07 07.0	
J011049−731428	01 10 49.61 −73 14 28.2	
J011132−730209	01 11 32.25 −73 02 09.9	
J045551−690209	04 55 51.56 −69 02 09.5	
J045608−701433	04 56 08.67 −70 14 33.3	
J050551−695116	05 05 51.89 −69 51 16.5	
J051129−680618	05 11 29.40 −68 06 18.1	
J051222−673220	05 12 22.54 −67 32 20.5	
J051537−672128	05 15 37.36 −67 21 28.4	
J051832−693520	05 18 32.48 −69 35 20.6	
J052635−674909	05 26 35.05 −67 49 09.2	
J054317−662655	05 43 17.54 −66 26 55.8	
J054750−672801	05 47 50.02 −67 28 01.8	

Note. H II = H II region, PWN = pulsar wind nebula. Objects in the LMC and SMC regions which we classified as background sources are also listed.

5.4 Galactic sources

The Galactic plane $b < 1°\!.5$ was excluded from the main AT20G follow-up. However, as part of our analysis some sources at higher Galactic latitude have been identified as Galactic Planetary Nebulae or H II regions. These have been identified in the source catalogue (with flags p and h, respectively) to allow them to be excluded from extragalactic studies.

The 65 sources identified as PNe were found by looking for flat spectrum sources that were slightly extended, in terms of the 6 km visibility data. A full analysis including these data will be published separately. The 6 H II regions were identified through a search of the literature.

6 COMPLETENESS AND RELIABILITY

The overall completeness of the AT20G catalogue is a function of both the completeness of the original scanning survey, and the completeness of the follow-up survey. The methods for estimating completeness for both surveys are discussed in this section. In Section 7, we compare our catalogue with the Wright et al. (2009) *WMAP* catalogue to assess completeness and reliability.

6.1 Scanning survey completeness

In order to estimate the completeness of the survey catalogue (the catalogue of candidate sources that was used as a basis for the follow-up observations), false point sources with known brightness and positions were inserted into the time-ordered uncalibrated scans. The false sources were injected by taking the primary calibrator observation, scaling it to the correct flux and declination, applying an inverse calibration appropriate to the time of the observation and adding this to the raw data. The data were then processed using the same machinery that created the initial sky maps and a list of candidate sources, including the injected sources, was then detected. Finally, the extracted sources were compared to the list of input sources to measure the fraction of sources recovered as a function of flux density. Further details of this process are discussed in Hancock et al. (in preparation).

This process allowed us to assess the completeness for point sources. The AT20G survey is not sensitive to sources with angular sizes much larger than 45 arcsec and so our catalogue will be incomplete for extremely extended sources. This brightness sensitivity limit means that the AT20G survey cannot detect the emission from most nearby spiral galaxies, even those with integrated flux densities above 100 mJy at 20 GHz. The nearby spiral NGC 253 is detected as an extended AT20G source (J004733−251717) with a 20 GHz flux density of 608 mJy, and in this case the observed emission appears to arise from a central starburst rather than an AGN (see Tingay 2004; Brunthaler et al. 2009). At $z = 0.0008$ ($d = 3.3$ Mpc), NGC 253 is the lowest redshift galaxy detected in the AT20G survey. Although several other spiral galaxies are detected, including NGC 1068 (J024240−000046; $z = 0.0038$), NGC 4594 (J123959−113721; $z = 0.0036$) and NGC 4945 (J130527−492804;
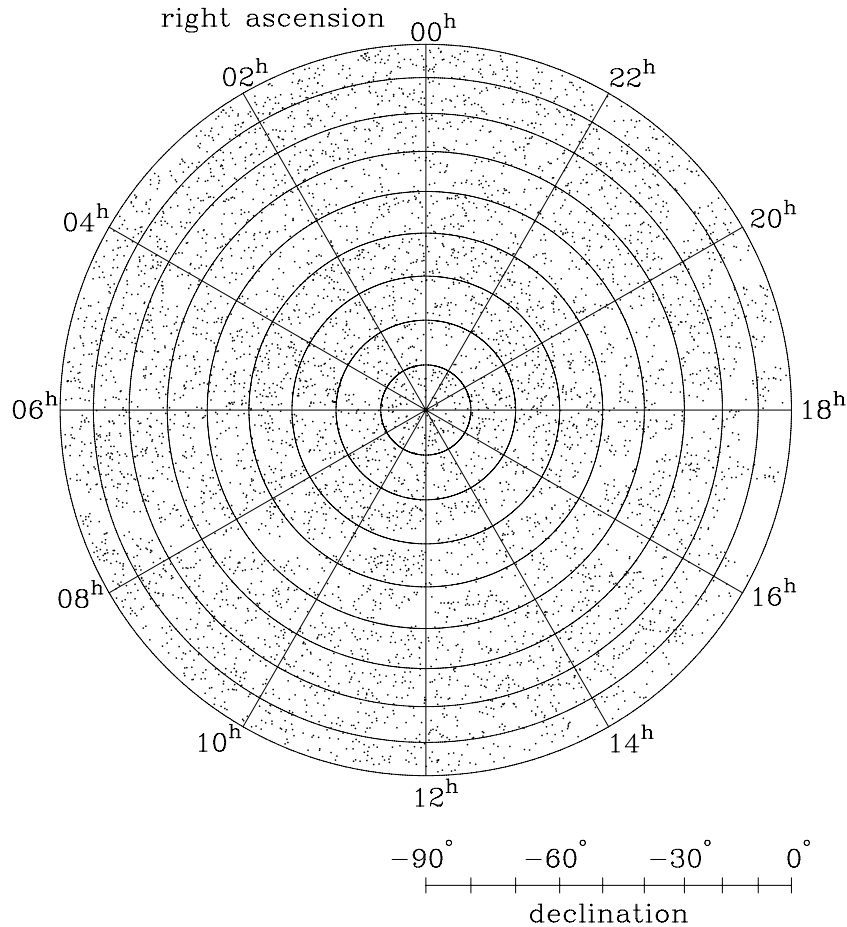
Figure 8. A plot in the equal-area Lambert projection showing the distribution of the 5890 sources in the AT20G catalogue. Note that the catalogue excludes the Galactic plane ($b < 1°5$) and that some regions north of $\delta = -15°$ are incomplete due to bad weather.

$z = 0.0019$), the detected radio emission in these galaxies appears to be associated mainly with an active nucleus rather than processes related to star formation.

6.2 Follow-up survey completeness

The completeness of the follow-up survey is a function of the completeness of the scanning survey catalogue and of the number of objects that were scheduled and observed in follow-up mode. The number of sources that we were able to observe was limited by the finite length of the project and the weather conditions during each observing run. The brightest sources in each region of the sky were observed first so as to maximize the number of sources confirmed and thus conserve the completeness of the follow-up observations. Bad weather and occasional hardware malfunctions meant that even though a source was scheduled for observation no good data were obtained. Much of these missing data were able to be recouped at a later stage via clean-up observations, but not all.

Fig. 8 shows the source distribution for the AT20G follow-up survey source catalogue. We calculated the follow-up survey completeness (C_f) using

$$C_f = \frac{C_s n_f}{n_s}, \tag{6}$$

where C_s is the completeness of the scanning survey (estimated using the source injection method described above), n_f is the number of sources detected in the follow-up survey and n_s is the number of real sources expected from the scanning survey. Note that the flux densities determined from the original scanning survey were accurate to ~ 20 per cent. Hence, towards the flux density cut-off there is a reduction in completeness due to some sources being omitted from the original candidate lists.

For regions south of $\delta = -15°$, we estimate the survey completeness to be 91 per cent above 100 mJy and 79 per cent above 50 mJy. The region $-15° < \delta < 0°$ is notably less complete than the rest of the survey. This region was observed last and was hampered by bad weather. We had several catch-up runs but this was not enough to fill in the missing area within the time limits we had set for near-simultaneous follow-up. The main region this affected was between 14 and 20 h in right ascension. A full analysis of the completeness statistics, including values for each declination band with ~ 2 h right ascension zones, will be presented in Massardi et al. (in preparation).

Since every object detected in the follow-up survey passed extensive quality control criteria, in addition to visual inspection, the reliability of the catalogue is essentially 100 per cent.

7 COMPARISON WITH THE *WMAP* 5-YEAR SOURCE CATALOGUE

Foreground point-source removal is an important step in the analysis of CMB anisotropy data, since the strongest sources need to be identified and masked out of the CMB images. The *WMAP* team

has therefore produced a catalogue of bright point sources in the *WMAP* sky maps at 23, 33, 41, 61 and 94 GHz (Wright et al. 2009) so that these can be masked out for the CMB analysis.

Since the AT20G survey overlaps in frequency with the lowest *WMAP* band (20–25 GHz), and the AT20G has significantly better sensitivity and resolution than the *WMAP* images, the AT20G catalogue provides an independent check of the completeness and reliability of the *WMAP* point-source catalogues.

Massardi et al. (2009) have recently published a detailed analysis which uses data from the AT20G BSS (Massardi et al. 2008) to evaluate several different strategies for foreground source detection in the *WMAP* 5-year maps. The release of the full AT20G catalogue will allow similar studies to push below the 0.5 Jy BSS limit and provide deeper complete samples for *Planck* and other CMB experiments.

A detailed comparison of the AT20G and *WMAP* source catalogues is beyond the scope of this paper, so we focus here on two questions: (i) what is the completeness and reliability of the *WMAP* source catalogue? and (ii) how consistent are the AT20G and *WMAP* flux density scales at 20–25 GHz?

7.1 Matching the AT20G and *WMAP* source catalogues

The *WMAP* 5-year source catalogue (Wright et al. 2009) contains 390 sources, of which 186 are in the Southern hemisphere. Wright et al. (2009) note that the *WMAP* catalogue is expected to be complete for sources stronger than 2 Jy in regions of the sky away from the Galactic plane, but also contains some sources with flux densities as low as 0.5 Jy at 23 GHz (*WMAP K* band)[6].

In matching the final AT20G catalogue with the *WMAP* 5-year source catalogue, we adopted the same 21.35 arcmin cut-off radius used by Massardi et al. (2008) for the AT20G BSS. 180 of the 186 southern sources in the *WMAP* catalogue were matched with at least one AT20G source within this 21.35 arcmin radius. Based on our determination of the surface density of bright AT20G sources, we expect all these matches to be genuine associations.

In 16 cases (i.e. 9 per cent of the *WMAP* source catalogue), two or more AT20G sources make a significant (>10 per cent) contribution to the total flux density in the 0°.93 *WMAP* beam at 23 GHz. Some of these correspond to AT20G detections of several components (e.g. core and hotspot, or two hotspots) of a single extended radio galaxy, while others appear to be unrelated pairs of sources.

Fig. 9 shows the offsets between the AT20G and *WMAP* positions for sources in common. In general, these are consistent with the quoted position errors (typically ∼4 arcmin for *WMAP* and less than 1 arcsec for AT20G). As expected, the offsets are generally smaller for stronger *WMAP* sources.

7.2 Completeness and reliability of the *WMAP* 5-year source catalogue

A simple comparison of surface densities shows that the *WMAP* and AT20G catalogues have similar levels of completeness for strong (>1.0 Jy) sources at 20–25 GHz. The surface density of sources stronger than 1.0 Jy is 28.5 ± 2.2 sr^{-1} for AT20G and 26.8 ± 1.7 sr^{-1} for the *WMAP K* band, where the quoted errors are set by the sample

Figure 9. Offset between AT20G and *WMAP* positions for southern sources in the 5-year *WMAP* source catalogue (Wright et al. 2009). Open circles show *WMAP* sources that were matched to a single AT20G source, and filled circles represent objects in which more than one AT20G source makes a significant (>10 per cent) contribution to the flux density in the *WMAP* beam at 23 GHz.

size in each case.[7] Since the *WMAP* surface density at 23 GHz is 94 per cent of the AT20G value, and the AT20G catalogue is essentially complete for point sources strong than 1 Jy, we estimate that the *WMAP* catalogue is roughly 94 per cent complete above 1 Jy at 23 GHz. Excluding the area masked in the *WMAP* source catalogue, we find only one strong (>1.5 Jy) AT20G source which is not listed in the *WMAP* catalogue, AT20G J142432−491349.

Appendix A lists the eight sources in the *WMAP* catalogue which have no AT20G match stronger than 250 mJy within 21.35 arcmin of the *WMAP* position. Three of these (the radio galaxy Fornax A, a Galactic H II region and the Galactic planetary nebula NGC 7293) are highly extended sources which are resolved out by the 2 arcmin ATCA beam, and so represent an incompleteness in the AT20G sample. Two sources are found in both surveys but with a very large position offset, and three sources catalogued by *WMAP* are not confirmed by AT20G and appear to be spurious. In general, however, there is very good agreement between the AT20G and *WMAP* source catalogues. Since the AT20G catalogue is essentially 100 per cent reliable, and ∼98 per cent of 23 GHz *WMAP* sources are matched in AT20G, we conclude that the 23 GHz *WMAP* catalogue is ∼98 per cent reliable.

---

[6]Wright et al. (2009) note that sources with flux densities below 1 Jy are unlikely to be detected by the *WMAP* unless they have 'benefited' from a positive noise or CMB fluctuation. This in turn leads to a bias in the *WMAP* catalogue at low flux densities (see e.g. Eddington 1913; Jauncey 1968).
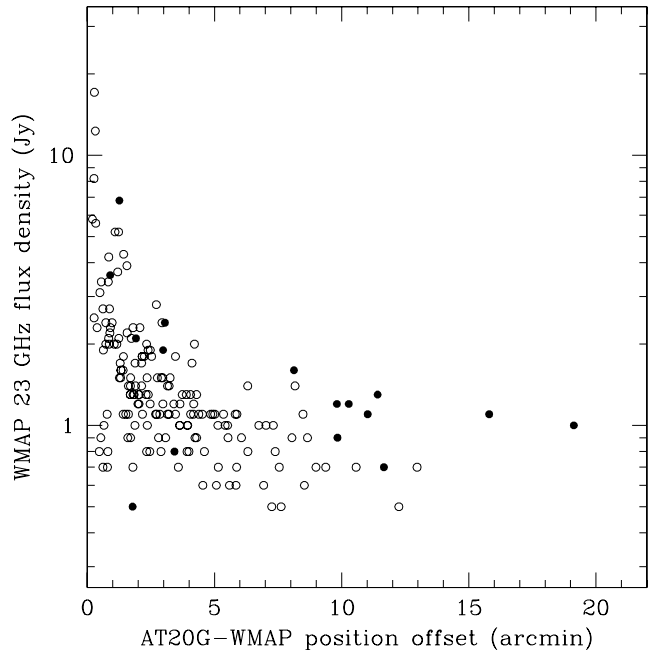
[7]The 5-year *WMAP* catalogue covers 78 per cent of the sky (the remaining 22 per cent, at low Galactic latitude, is masked out) and lists 262 sources with 23 GHz flux densities $\geq$1.0 Jy beam^{-1} and 123 sources with flux density $\geq$1.5 Jy beam^{-1}. The AT20G catalogue covers 48 per cent of the sky (declination < 0° with the region $b < 1°.5$ masked out) and lists 174 sources with 20 GHz flux densities $\geq$1.0 Jy beam^{-1} and 85 sources with flux density $\geq$1.5 Jy beam^{-1}.
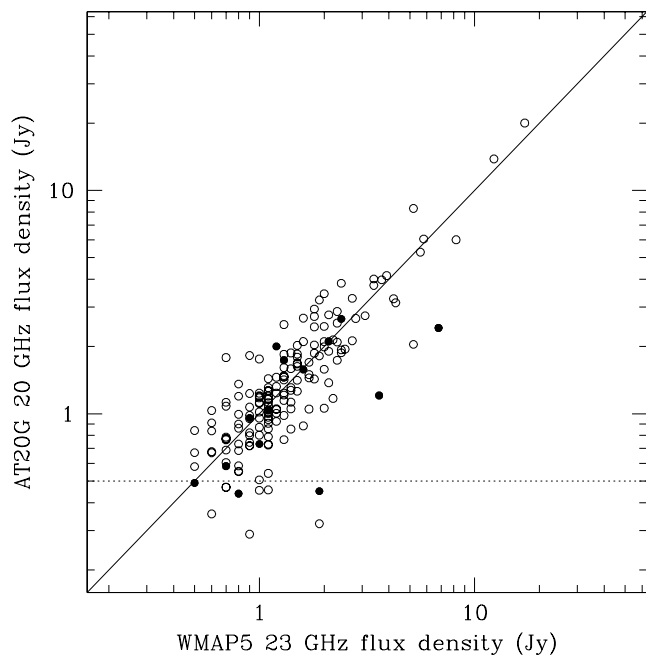
Figure 10. Comparison of AT20G (20 GHz) and *WMAP* (23 GHz) flux densities. As in Fig. 9, open circles represent *WMAP* sources matched to a single AT20G source and filled circles represent objects with two or more AT20G sources in the *WMAP* beam. The horizontal dashed line shows the 0.5 Jy limit of the AT20G BSS (Massardi et al. 2008).

7.3 Comparison of the AT20G and *WMAP* flux density scales

Fig. 10 compares the catalogued AT20G (20 GHz) and *WMAP* (23 GHz) flux densities for the 180 sources in common.

To test for consistency of the AT20G and *WMAP* flux-density scales, we compared the flux densities of the 119 sources which were stronger than 1.0 Jy in the *WMAP* catalogue (to minimize measurement errors) and had only a single AT20G counterpart (to exclude extended sources for which the AT20G flux densities may be underestimated). For these sources, we find a mean flux ratio

$$\left\langle \frac{S_{AT20G}}{S_{WMAP}} \right\rangle = 1.01 \pm 0.03 \ . \tag{7}$$

The rms scatter of the individual fluxes is 0.31. The main contribution to the standard deviation in the flux ratios probably comes from variability, since the AT20G and *WMAP* measurements are generally not simultaneous. The typical uncertainty in the individual *WMAP* and AT20G flux density measurements is 4–5 per cent. Since the formal standard error on the mean flux ratio is 0.028, we conclude that the AT20G and *WMAP* flux density scales are consistent to within 2–3 per cent at 20–25 GHz.

8 ANALYSIS

8.1 Polarization

To test the robustness of our polarization measurements, we used the variability sample (see Section 2.5), selecting a set of 142 objects which had good quality observations in our 2004 October, 2005 October and 2006 April observing epochs. Fig. 11 shows the fractional polarization at 20 GHz for the 2005 October versus 2004 October observations. Crosses show measured polarization values,
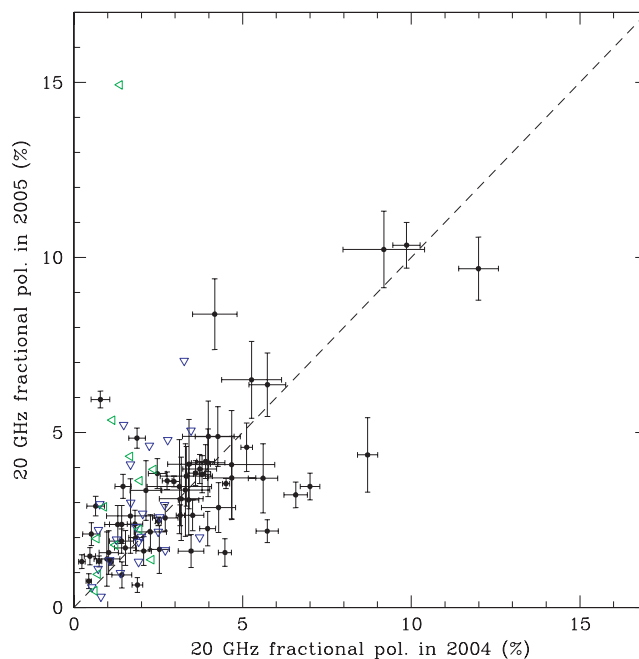

Figure 11. Comparison of fractional polarization at 20 GHz measured in our 2004 October and 2005 October observing runs. Crosses show measured polarization values, and triangles show limits in one of the epochs.
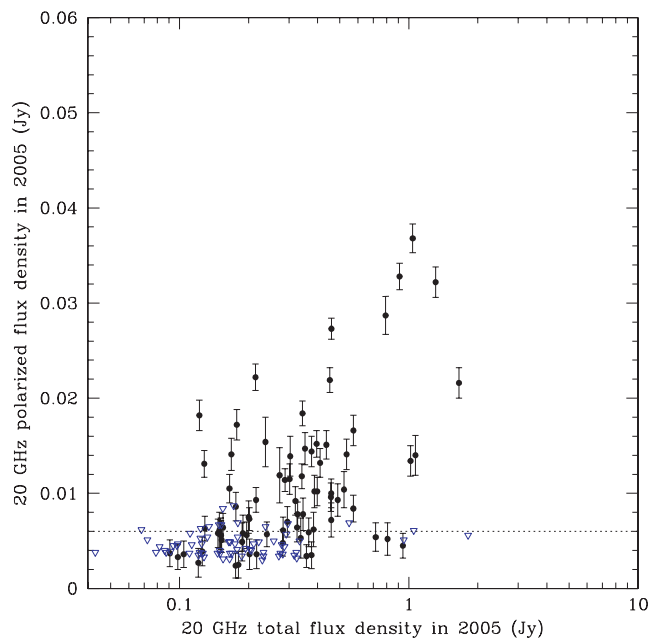

Figure 12. Polarized flux density versus total flux density at 20 GHz for the 2005 October observing run. Crosses show measured polarization values, and triangles show limits.

and triangles show limits in one of the epochs. There is good correlation (albeit with significant scatter) between each pair of epochs.

Fig. 12 shows the 20 GHz polarized intensity versus the total flux density for variability sample sources observed in 2005 October. The dashed horizontal line shows a 6 mJy limit in polarized flux, a level three to four times the typical error in polarized flux. Most of the limits (triangles) fall below this line, and so it was chosen
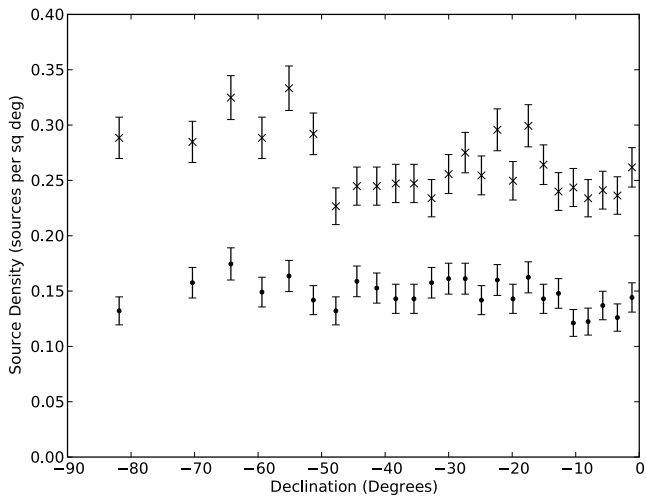
© 2010 The Authors. Journal compilation © 2010 RAS, MNRAS **402,** 2403–2423

Figure 13. Source density in equal-area declination bands. Circles and crosses show sources above a 100 and 50 mJy cut-off, respectively. Errors are Poissonian. At a 50 mJy cut-off, we have regions of incompleteness (notably $0°$ to $-15°$ and $-30°$ to $-50°$), as discussed in the text.

Figure 14. $\log(N) - \log(S)$ source counts at 20 GHz, with Poisson errors. These are well fit by a power law down to $\sim$100 mJy where the turnover indicates incompleteness.

as a reasonable level at which the polarized flux density can be reliably determined (see Section 3.5). Although a small number of sources have a measured polarized flux density below 6 mJy, further investigation found that these detections were near the 3σ detection limit, and hence were not highly reliable.

The triangle in the upper left of Fig. 11 corresponds to source J084225–605350, which appeared highly polarized in 2005 (polarized flux 18 ± 1 mJy, fractional polarization 5.4 per cent) and 2006 (16 ± 3 mJy, fractional polarization 4.0 per cent) but not in 2004 (<6 mJy, fractional polarization <1.7 per cent). This deserves further investigation, as it raises the possibility that some AT20G sources may be genuinely variable in polarized flux.

We found a good correlation between the fractional polarization measured at 5 and 8 GHz, and also a reasonable correlation between the fractional polarization measured at 5 and 20 GHz, although the large scatter in the latter case suggests that there may be some change in the polarization properties of the sources across the wider frequency range. There was also reasonable consistency in polarized position angles measured at each of the three frequencies. This will be analysed in more detail in Massardi et al. (in preparation).

8.2 Source counts

Fig. 13 shows the 20 GHz source density with in equal-area declination bands, for flux density cut-offs of 100 and 50 mJy. It shows that we have relatively homogeneous coverage of the southern sky down to 100 mJy. At a 50 mJy cut-off, we have regions of incompleteness (notably $0°$ to $-15°$ and $-30°$ to $-50°$) as discussed in Section 6. This is primarily due to bad weather in the follow-up runs.

Fig. 14 shows a plot of the AT20G differential source counts [log $(N) - \log(S)$]. These are well fit by a power law [$f(x) = 31x^{-2.15}$] down to $\sim$100 mJy where the flattening of the curve is a sign that the catalogue is becoming incomplete at this level. This agrees with our analysis in Section 6. Note that the source counts presented here are not corrected for completeness – this will be explored further in Massardi et al. (in preparation).
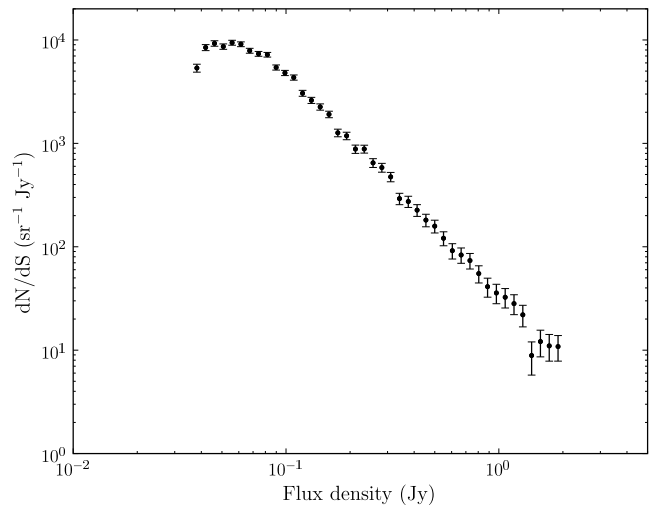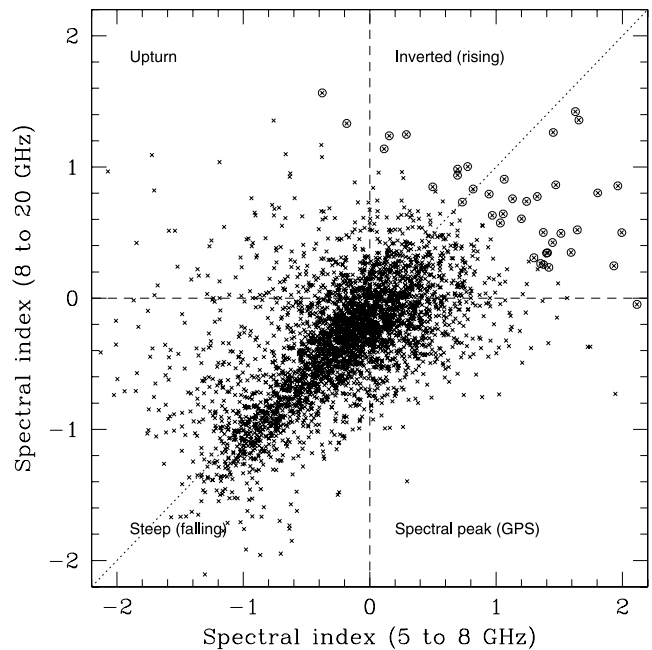

Figure 15. Radio two-colour diagram. Crosses show AT20G sources observed at all three frequencies. Open circles show the UIS sources with a spectral index of $\alpha(5, 20) > +0.7$. These sources are discussed in Section 8.4.

8.3 Spectral index distribution

In low-frequency radio surveys, a commonly used diagnostic is the spectral index:

$$\alpha(\nu_1, \nu_2) = \frac{\log(S_1/S_2)}{\log(\nu_1/\nu_2)}, \tag{8}$$

where S_1 is the flux density measured at frequency ν_1 and likewise for S_2 and ν_2.

The spectral index is only valid over frequency ranges in which the effects of spectral curvature can be ignored, which is clearly not the case for the AT20G sample. Hence, for our analysis it is more appropriate to use a radio colour–colour diagram (e.g. Kesteven, Bridle & Brandie 1977; Sadler et al. 2006). Fig. 15 shows a

colour–colour plot for the 3763 AT20G sources with near-simultaneous data at 5, 8 and 20 GHz. The plot compares the lower frequency spectral index $\alpha(5, 8)$ with the higher frequency spectral index $\alpha(8, 20)$.

As noted previously by Sadler et al. (2006) and Massardi et al. (2008), this plot shows a wide range of spectral types at 20 GHz. Four main types can be identified.

(i) Sources with steep (falling) spectra, which are shown in the lower-left quadrant. These represent ∼57 per cent of the sample and include a higher fraction of power-law spectra.

(ii) Sources with peaked spectra, which rise at lower frequencies and fall at higher frequencies. These are shown in the lower-right quadrant and represent ∼21 per cent of the sample.

(iii) Sources with inverted (rising) spectra, which are shown in the upper-right quadrant. These make up ∼14 per cent of sources.

(iv) Sources with an upturn in their spectra, shown in the upper-left quadrant. These represent ∼8 per cent of the sample.

The diagonal line indicates sources whose spectrum can be represented by a single power law. More sources lie below this line than above it, suggesting that most sources steepen with increasing frequency. For the flat spectrum sources in particular, there is no evidence for power-law spectra. This demonstrates that high-frequency flux densities cannot be reliably estimated from low-frequency surveys by extrapolating from a single power-law spectrum.

We have also identified a new class of sources with ultra-inverted spectra [$\alpha(5, 20) > +0.7$]. These are shown as open circles in Fig. 15 and discussed in the next section.

8.4 Low-frequency catalogues and ultra-inverted spectrum radio sources

To test whether the AT20G survey has found any new radio-source population not seen at lower frequency, we cross-matched the AT20G catalogue with the 1.4 GHz NVSS (Condon et al. 1998) and 843 MHz SUMSS (Mauch et al. 2003) and the 2nd-epoch Molonglo Plane Survey (MGPS-2; Murphy et al. 2007) surveys, which together cover the whole AT20G survey area. The 40 mJy cut-off of the AT20G catalogue is an order of magnitude brighter than the NVSS and SUMSS/MGPS-2 completeness limits (which are typically 2.5–10 mJy, depending on declination), so we expect the vast majority of AT20G sources to have an NVSS or SUMSS match within 10–15 arcsec on the sky. AT20G sources without a counterpart in the NVSS and SUMSS catalogues must have either a sharply rising radio spectrum (with $\alpha > +0.5$) or highly variable radio emission.

Our cross-matching identified 27 AT20G sources (0.4 per cent of the AT20G catalogue) with no counterpart in the NVSS and SUMSS/MGPS-2 catalogues, and these are listed in Table 8. For 11 of them, examination of the original NVSS and SUMSS survey images shows a weak source at the AT20G position – these objects are detected at the 3σ level but fall below the NVSS/SUMSS

Table 8. AT20G sources without a low-frequency counterpart in the SUMSS or NVSS catalogue. The (near-simultaneous) AT20G spectral index between 5 and 20 GHz is also listed. Optical B(J) identifications and magnitudes are from the SuperCOSMOS catalogue (Hambly et al. 2001), and infrared K magnitudes from the Two-Micron All-Sky Survey (2MASS) Extended Source Catalogue (Jarrett et al. 2000). The redshift of J052755−471828 has been measured by Drake, McGregor & Dopita (2004) and the redshift of J094258−604621 by Radburn-Smith et al. (2006). The median 20 GHz flux density of the sources in this table is 72 mJy.

| AT20G name | Flux density (mJy) | | | | | $\alpha(1, 20)$ | $\alpha(5, 20)$ | $\pm$ | Optical ID | Comment |
	S_{20}	S_8	S_5	NVSS	SUMSS					
J023611−420337	95	75	36	–	7.3	+0.81	+0.68	0.07	Faint/blank	No obvious optical ID
J030406−450342	59	49	26	–	<3.3	> +0.90	+0.57	0.09	QSO?	Stellar ID, B(J) = 18.0 mag
J032945−485420	40	58	47	–	<3.3	> +0.79	−0.11	0.08	QSO?	Stellar ID, B(J) = 19.1 mag
J034258−431813	97	97	39	–	9.4	+0.74	+0.64	0.09	QSO?	Stellar ID, B(J) = 18.4 mag
J044023−473218	61	21	9	–	<3.3	> +0.92	+1.34	0.12	Faint/blank	Possible faint ID, B(J) = 22.7 mag
J052755−471828	106	–	–	–	9.9	+0.75	–	–	Galaxy	2MASS galaxy B = 13.0 mag, B = 0.134
J054417−641914	123	66	32	–	<3.3	> +1.14	+0.94	0.08	Faint/blank	Crowded field near LMC, no obvious ID
J070949−381152	86	33	6	<2.5	<5.1	> +1.33	+1.87	0.15	Galaxy	2MASS galaxy with K = 12.7 mag
J073040−544152	70	–	–	–	<7.5	> +0.70	–	–	Faint/blank	Low S/N in SUMSS image, no obvious ID
J080931−472011	86	50	27	–	7.7	+0.76	+0.81	0.09	–	Low Galactic latitude, $b = -7°.7$
J094258−604621	51	33	23	–	8.7	+0.56	+0.59	0.06	Galaxy	2MASS galaxy K = 12.9 mag, z = 0.096
J095159−183703	70	71	38	<3.3	–	> +1.15	+0.43	0.08	Faint/blank	No obvious optical ID
J104227−210556	58	–	–	<2.0	–	> +1.27	–	–	Faint/blank	No obvious optical ID
J111015−665531	136	66	21	–	6.0	+0.99	+1.31	0.07	QSO?	Stellar ID B(J) = 19.1 mag
J111246−203932	78	30	6	<2.0	–	> +1.38	+1.80	0.17	Faint/blank	No obvious optical ID
J111605−263758	40	5	3	<1.2	–	> +1.32	+1.82	0.34	Faint/blank	No obvious optical ID
J114844−781933	124	63	22	–	<5.0	> +1.01	+1.21	0.07	Galaxy	B(J) = 18.5 mag galaxy
J123229−840247	48	86	79	–	6.3	+0.64	−0.35	0.08	Faint/blank	No obvious optical ID
J140257−664031	72	58	26	–	<5.0	> +0.84	+0.71	0.07	–	Low Galactic latitude, $b = -4°.8$
J161845−142428	84	–	–	<2.5	–	> +1.32	–	–	Faint/blank	No obvious optical ID
J171043−471820	76	–	–	–	6.8	+0.76	–	–	–	Low Galactic latitude, $b = -4°.4$
J173039−211112	54	–	–	<2.5	–	> +1.16	–	–	Faint/blank	No obvious optical ID
J181225−712006	43	39	26	–	5.2	+0.67	+0.35	0.09	Galaxy	2MASS galaxy K = 12.9 mag
J195906−755202	42	30	23	–	<3.5	> +0.78	+0.42	0.07	QSO?	Stellar ID, B(J) = 20.6 mag
J200012−474951	78	64	28	–	7.4	+0.74	+0.72	0.10	QSO?	Stellar ID, B(J) = 20.2 mag
J205503−635207	44	29	12	–	4.6	+0.71	+0.91	0.09	QSO?	Stellar ID, B(J) = 20.2 mag
J220413−465424	99	103	30	–	<4.0	> +1.01	+0.84	0.08	Faint/blank	No obvious optical ID

catalogue limit. For the remaining 16 objects, Table 8 lists a 3σ upper limit to the low-frequency NVSS/SUMSS flux density.

Recent results from the 15 GHz 9C survey also confirm a population of high-frequency sources that fall below the limits of low-frequency catalogues. At flux densities of 10–15 mJy, Waldram et al. (2009) find that 4.3 per cent of their 15 GHz sources are not listed in the NVSS.

All the sources in Table 8 have (non-simultaneous) 1–20 GHz spectral indices $\alpha(1, 20) > +0.7$. An obvious question is whether these extreme spectral indices are the result of source variability between the NVSS/SUMSS and AT20G observing epochs. This does not generally appear to be the case. The sources in Table 8 are also among the most extreme AT20G objects in terms of their (simultaneous) 5–20 GHz spectral index, with a median value of $\alpha(5, 20) = +0.68$ [the median $\alpha(5, 20)$ for the AT20G sample as a whole is -0.22]. In all but two cases (J032945−485420 and J123229−840247), the data in Table 8 are consistent with the existence of a population of objects with a rapidly rising power-law radio spectrum between 1 and 20 GHz and little or no variability on time-scales of up to a decade.

By analogy with the Ultra-Steep Spectrum radio sources with $\alpha < -1.3$ (Blumenthal & Miley 1979; Tielens, Miley & Willis 1979), we introduce the term 'Ultra-Inverted Spectrum (UIS) radio

Table 9. UIS AT20G sources with 5–20 GHz spectral index $\alpha \geq +0.7$.

AT20G Name	J2000 RA	Dec.	S_{20}	$\pm$	S_8	$\pm$	S_5	$\pm$	$\alpha(5, 20)$	$\pm$	Notes
J002616−351249	00 26 16.40	−35 12 49.3	1123	43	357	18	136	7	+1.48	0.06	PMN J0026−3512, He07
J011102−474911	01 11 02.93	−47 49 11.3	83	4	64	3	30	2	+0.71	0.08	$z = 0.154$ galaxy, 2dFGRS
J012457−511316	01 24 57.38	−51 13 16.0	745	37	369	19	229	11	+0.83	0.07	PKS 0122−514, He07
J024709−281049	02 47 09.00	−28 10 49.7	133	9	108	6	35	2	+0.94	0.09	
J025055−361635	02 50 55.42	−36 16 35.3	340	16	219	11	84	4	+0.98	0.07	$z = 1.536$ QSO, Su04
J042810−643823	04 28 10.87	−64 38 23.6	326	15	201	10	110	6	+0.76	0.07	PMN J0428−6438, He07
J043445−421108	04 34 45.34	−42 11 08.0	165	7	58	4	53	3	+0.80	0.07	PMN J0434−4211, He07
J044023−473218	04 40 23.75	−47 32 18.5	61	3	21	2	9	1	+1.34	0.12	
J050732−510416	05 07 32.51	−51 04 16.3	103	5	31	2	12	1	+1.51	0.10	$z = 0.522$ galaxy, St91
J051321−212821	05 13 21.17	−21 28 21.4	77	5	33	2	21	2	+0.91	0.12	$z = 0.355$ galaxy, 6dFGS
J054223−514257	05 42 23.47	−51 42 57.4	128	7	69	4	45	2	+0.73	0.07	
J054417−641914	05 44 17.81	−64 19 14.4	123	6	66	3	32	2	+0.94	0.08	
J070949−381152	07 09 49.68	−38 11 52.7	86	3	33	3	6	1	+1.87	0.15	$K = 12.7$ galaxy, 2MASS
J073940−291118	07 39 40.11	−29 11 18.2	122	8	80	4	25	2	+1.11	0.11	
J074109−544746	07 41 09.25	−54 47 46.1	86	5	39	2	26	2	+0.84	0.10	$K = 13.9$ galaxy, 2MASS
J080931−472011	08 09 31.97	−47 20 11.2	86	4	50	3	27	2	+0.81	0.09	
J083046−170635	08 30 46.57	−17 06 35.2	235	15	141	7	70	4	+0.85	0.09	
J083529−595311	08 35 29.00	−59 53 11.4	549	27	281	14	162	8	+0.86	0.07	PMN J0835−5953, He07
J095633−404454	09 56 33.21	−40 44 54.8	75	4	39	2	18	1	+1.00	0.08	
J101112−221644	10 11 12.80	−22 16 44.5	55	4	29	2	15	2	+0.91	0.15	PMN J1011−2216
J111015−665531	11 10 15.79	−66 55 31.9	136	6	66	3	21	1	+1.31	0.07	
J111246−203932	11 12 46.81	−20 39 32.1	78	5	30	2	6	1	+1.80	0.17	
J111605−263758	11 16 05.96	−26 37 58.5	40	3	5	1	3	1	+1.82	0.34	
J114844−781933	11 48 44.32	−78 19 33.6	124	6	63	3	22	1	+1.21	0.07	
J132649−525623	13 26 49.23	−52 56 23.6	2061	103	1350	68	606	30	+0.86	0.07	PMN J1326−5256
J140257−664031	14 02 57.40	−66 40 31.3	72	4	58	3	26	1	+0.71	0.07	
J143608−153609	14 36 08.09	−15 36 09.1	113	6	53	3	10	1	+1.70	0.11	
J144555−303705	14 45 55.96	−30 37 05.5	241	12	105	5	70	5	+0.87	0.09	PMN J1445−3036, He07
J151726−261820	15 17 26.60	−26 18 20.8	219	14	107	9	80	8	+0.71	0.12	PMN J1517 − 2618,He07
J153030−220811	15 30 30.91	−22 08 11.8	78	6	35	3	8	5	+1.60	0.74	
J153744−295433	15 37 44.26	−29 54 33.6	133	7	93	5	40	3	+0.84	0.09	
J154644−683728	15 46 44.52	−68 37 28.8	506	25	135	7	168	8	+0.77	0.07	PMN J1546−6837, He07
J155205−242521	15 52 05.39	−24 25 21.5	139	9	104	6	46	4	+0.77	0.11	PMN J1552−2425, He07
J161434−354329	16 14 34.01	−35 43 29.6	243	11	93	6	87	5	+0.72	0.07	
J171651−470247	17 16 51.68	−47 02 47.1	129	6	45	4	38	3	+0.86	0.09	
J172746−754617	17 27 46.16	−75 46 17.9	67	3	50	3	22	1	+0.78	0.06	
J183923−345348	18 39 23.56	−34 53 48.5	313	16	151	8	64	3	+1.11	0.07	
J191816−411131	19 18 16.06	−41 11 31.3	357	16	116	6	129	7	+0.71	0.07	PMN J1918−4111, He07
J195949−441611	19 59 49.32	−44 16 11.1	172	9	80	4	43	2	+0.97	0.07	PMNM 195617.0−442457
J200012−474951	20 00 12.95	−47 49 51.5	78	5	64	3	28	2	+0.72	0.10	
J204107−524242	20 41 07.70	−52 42 42.6	55	3	44	3	20	1	+0.71	0.08	PMN J2041−5242
J205503−635207	20 55 03.83	−63 52 07.0	44	2	29	2	12	1	+0.91	0.09	
J210457−201101	21 04 57.07	−20 11 01.8	102	6	76	4	30	3	+0.86	0.12	PMN J2105−2011
J220413−465424	22 04 13.06	−46 54 24.7	99	5	103	5	30	2	+0.84	0.08	
J231347−441615	23 13 47.91	−44 16 15.3	138	7	81	5	46	3	+0.77	0.08	

Notes. 'He07' in the Notes column indicates a source which is also in the CRATES sample of Healey et al. (2007). Identifications and redshifts are from the NED. Redshift references are: Su04 = Sulentic et al. (2004); St91 = Stocke et al. (1991); 6dFGS = Jones et al. (2009) and 2dFGRS = Colless et al. (2001). The strongest source in this table J132649−525623 (=PMN J1326−5256) has been observed to show intra-day variability at 6.6 GHz (McCulloch et al. 2005).
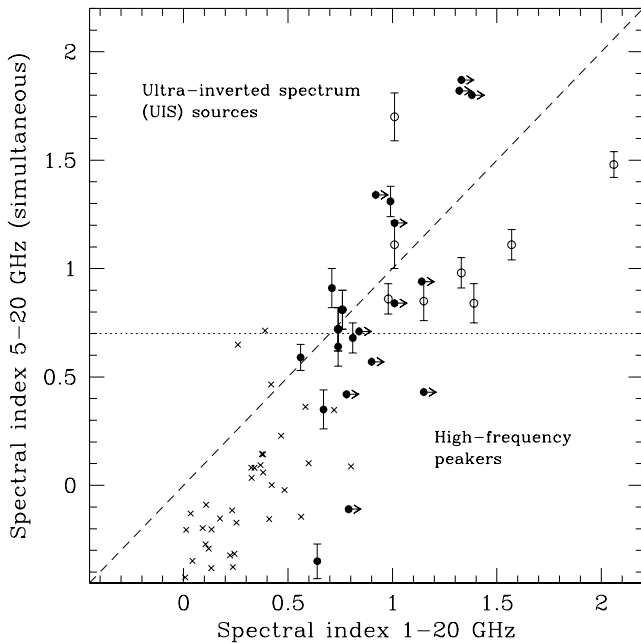
Figure 16. Comparison of 1–5 and 5–20 GHz spectral indices for the sources in Table 8 (filled circles) and the 'HFP' sample of Dallacasa et al. (2000) (crosses). Open circles show AT20G UIS sources (Table 9) which have both $\alpha(5, 20) > +0.7$ and $\alpha(1, 20) > +0.7$.

source' to describe the class of radio sources with a spectral index $\alpha(5, 20) > +0.7$.

The AT20G catalogue contains 45 sources with $\alpha(5, 20) > +0.7$ (roughly 1.2 per cent of the AT20G sources with 5 and 8 GHz data), and these are listed in Table 9. A few of these sources are detected in linear polarization, confirming that the emission mechanism is non-thermal, so we assume for now that all the AT20G UIS objects are extragalactic non-thermal sources. Further investigation is needed to confirm this, but we note that the UIS sources have the same distribution in Galactic latitude as the main AT20G sample and show no concentration towards the Galactic plane.

Fig. 16 compares the AT20G sources in Table 8 with the sample of high-frequency peakers (HFPs) studied by Dallacasa et al. (2000), who measured simultaneous flux densities at several frequencies between 1.4 and 22.5 GHz for a sample of 55 sources selected to have inverted spectra with $\alpha(1, 5) > +0.5$. Our AT20G UIS sources with $\alpha(5, 20) > +0.7$ have radio spectra which rise more rapidly with frequency than any of the HFP sample. If the AT20G UIS sources peak at frequencies near or above 20 GHz, the O'Dea (1998) relation between spectral peak and source size implies that these are expected to be very young, compact radio sources less than a few tens of parsec in size.

Only a handful of similarly extreme inverted-spectrum radio sources have previously been identified. They include the $z = 0.089$ galaxy III Zw 2 (Falcke et al. 1999; Brunthaler et al. 2003) and the $z = 0.644$ quasar RXJ 1415+3337 (Orienti & Dallacasa 2008). Falcke et al. (1999) measured a spectral index of $\alpha = +1.9 \pm 0.1$ between 5 and 10 GHz for III Zw 2, with a spectral peak near 40 GHz, while RXJ 1415+3337 has $\alpha = +0.9$ between 1 and 22 GHz. Both sources show an evolution of the radio spectrum over time-scales of several years, with the spectral peak slowly moving to lower frequencies, and III Zw 2 can be modelled in terms of a single, adiabatically expanding homogeneous radio component (Orienti & Dallacasa 2008).

8.5 Optical identifications

Optical counterparts of the full AT20G sample were found by cross-matching the radio positions with optical positions in the Super-COSMOS data base (Hambly et al. 2001). AT20G objects within $10°$ of the Galactic plane were excluded from this analysis due to the presence of foreground stars and Galactic dust extinction, leaving a total of 4932 objects used in this analysis. Optical identifications were chosen to be the closest optical source to the radio position within a 2.5 arcsec radius and brighter than a *B* magnitude of 22, which is the SuperCOSMOS completeness limit. Previous studies have found that 97 per cent of sources selected in this way are likely to be genuine associations (Sadler et al. 2006).

Using this selection method, there are 2958 AT20G sources (60 per cent) with optical identifications, the majority of which are quasi-stellar objects (QSOs). This is much higher than seen in low-frequency radio surveys which typically have an optical identification rate of 25–30 per cent. This again highlights the significant difference of the AT20G source population from other radio-selected AGN samples. Full analysis of the optical properties of these objects will be published separately (Mahony et al. in preparation)

9 CONCLUSIONS AND FUTURE WORK

We present a catalogue of 5890 sources from the AT20G, the deepest large-area survey at high radio frequency. For 3766 of these sources, we have near-simultaneous 5 and 8 GHz measurements, and 1559 sources have a detection in polarized total intensity at one or more of the three frequencies.

The 20 GHz flux densities measured for the strongest AT20G sources are in excellent agreement with the *WMAP* 5-year source catalogue recently published by Wright et al. (2009), and we find that the *WMAP* source catalogue is close to complete (and highly reliable) for sources stronger than 1.5 Jy at 23 GHz.

We identify a population of UIS radio sources with a spectral index of $\alpha(5, 20) > +0.7$. These are rare sources, comprising roughly 1.2 per cent of the AT20G population.

There are several ongoing projects as part of the AT20G. Massardi et al. (in preparation) will present a statistical analysis of the AT20G sources, and Hancock et al. (in preparation) will present results from the original scanning survey. Mahony et al. (in preparation) are carrying out an analysis of the optical identifications of AT20G sources. Sadler et al. (2008) are following up subsamples of the AT20G sources at 95 GHz. Murphy et al. (2009) are targeting a subset of Galactic sources that were excluded from the main follow-up survey. Chhetri et al. (in preparation) have carried out a search for gravitational lens candidates and planetary nebulae using data from the 6 km baseline. In a related project, Sadler et al. (in preparation) are conducting a deeper survey at 20 GHz to explore the high-frequency radio population at much lower flux densities.

is part of the Australia Telescope which is funded by the Commonwealth of Australia for operation as a National Facility managed by the CSIRO.

This research has made use of the NED which is operated by the Jet Propulsion Laboratory, California Institute of Technology, under contract with the National Aeronautics and Space Administration.

We thank the referee, Jim Condon, for his useful feedback.

REFERENCES

Bennett C. L., Hill R. S., Hinshaw G. et al., 2003, ApJS, 148, 97
Blumenthal G., Miley G., 1979, A&A, 80, 13
Brunthaler A., Falcke H., Bower G. C., Aller M. F., Aller H. D., Teräsranta H., Krichbaum T. P., 2003, Publ. Astron. Soc. Aust., 20, 126
Brunthaler A., Castangia P., Tarchi A., Henkel C., Reid M. J., Falcke H., Menten K. M., 2009, A&A, 497, 103
Burke-Spolaor S., Ekers R. D., Massardi M., Murphy T., Partridge B., Ricci R., Sadler E. M., 2009, MNRAS, 395, 504
Colless M., Dalton G., Maddox S. et al., 2001, MNRAS, 328, 1039
Condon J. J., Broderick J. J., Seielstad G. A., 1989, AJ, 97, 1064
Condon J. J., Cotton W. D., Greisen E. W., Yin Q. F., Perley R. A., Taylor G. B., Broderick J. J., 1998, AJ, 115, 1693
Dallacasa D., Stanghellini C., Centonza M., Fanti R., 2000, A&A, 363, 887
de Zotti G., Ricci R., Mesa D., Silva L., Mazzotta P., Toffolatti L., González-Nuevo J., 2005, A&A, 431, 893
Drake C. L., McGregor P. J., Dopita M. A., 2004, AJ, 128, 955
Eddington A. S., 1913, MNRAS, 73, 359
Falcke H., Bower G. C., Lobanov A. P. et al., 1999, ApJ, 514, L17
Fey A. L., Ma C., Arias E. F. et al., 2004, AJ, 127, 3587
Filipović M. D., Payne J. L., Reid W., Danforth C. W., Staveley-Smith L., Jones P. A., White G. L., 2005, MNRAS, 364, 217
Griffith M. R., Wright A. E., 1993, AJ, 105, 1666
Hambly N. C., MacGillivray H. T., Read M. A. et al., 2001, MNRAS, 326, 1279
Healey S. E., Romani R. W., Taylor G. B. et al., 2007, ApJS, 171, 61
Hinshaw G., Nolta M. R., Bennett C. L. et al., 2007, ApJS, 170, 288
Jarrett T. H., Chester T., Cutri R., Schneider S., Skrutskie M., Huchra J. P., 2000, AJ, 119, 2498
Jauncey D. L., 1968, ApJ, 152, 647
Jones D. H., Read M. A., Saunders W. et al., 2009, MNRAS, 399, 683
Kesteven M. J. L., Bridle A. H., Brandie G. W., 1977, AJ, 82, 541
Lo K. Y., Chiueh T. H., Martin R. N. et al., 2001, in Wheeler J. C., Martel H., eds, AIP Conf. Ser. Vol. 586, 20th Texas Symposium on Relativistic Astrophysics, AMiBA: Array for Microwave Background Anistropy. Am. Inst. Phys., New York, p. 172
Lortet M.-C., Borde S., Ochsenbein F., 1994, A&AS, 107, 193
McCulloch P. M., Ellingsen S. P., Jauncey D. L., Carter S. J. B., Cimò G., Lovell J. E. J., Dodson R. G., 2005, AJ, 129, 2034
Massardi M., Ekers R. D., Murphy T. et al., 2008, MNRAS, 384, 775
Massardi M., López-Caniego M., González-Nuevo J., Herranz D., de Zotti G., Sanz J. L., 2009, MNRAS, 392, 733
Mauch T., Murphy T., Buttery H. J., Curran J., Hunstead R. W., Piestrzynski B., Robertson J. G., Sadler E. M., 2003, MNRAS, 342, 1117
Middelberg E., Sault R. J., Kesteven M. J., 2006, Publ Astron. Soc. Aust., 23, 147
Moorey G. G., Bolton R. J., Bowen M. A. et al., 2008, in Hoogeboom P., Schreurs D., eds, 38th European Microwave Conference Cryogenically Cooled Millimetre-Wave Front Ends for the Australia Telescope. EUMA, Amsterdam, p. 155
Murphy T., Mauch T., Green A., Hunstead R. W., Piestrzynska B., Kels A. P., Sztajer P., 2007, MNRAS, 382, 382
Murphy T., Cohen M., Ekers R., Green A., Wark R., Moss V., 2009, MNRAS, in press
O'Dea C. P., 1998, PASP, 110, 493
Orienti M., Dallacasa D., 2008, A&A, 477, 807
Payne J. L., Filipović M. D., Reid W., Jones P. A., Staveley-Smith L., White G. L., 2004, MNRAS, 355, 44
Radburn-Smith D. J., Lucey J. R., Woudt P. A., Kraan-Korteweg R. C., Watson F. G., 2006, MNRAS, 369, 1131
Ricci R., Sadler E. M., Ekers R. D. et al., 2004, MNRAS, 354, 305
Sadler E. M., Ricci R., Ekers R. D. et al., 2006, MNRAS, 371, 898
Sadler E. M., Ricci R., Ekers R. D., Sault R. J., Jackson C. A., de Zotti G., 2008, MNRAS, 385, 1656
Sault R. J., 2003, ATNF Technical Report 39.3/124, ATCA flux density scale at 12mm. Australia Telescope National Facility, Sydney
Sault R. J., Teuben P. J., Wright M. C. H., 1995, in Shaw R. A., Payne H. E., Hayes J. J. E., eds, ASP Conf. Ser. Vol. 77, Astronomical Data Analysis Software and Systems IV, A Retrospective View of MIRIAD. Astron. Soc. Pac., San Francisco, p. 433
Stocke J. T., Morris S. L., Gioia I. M., Maccacaro T., Schild R., Wolter A., Fleming T. A., Henry J. P., 1991, ApJS, 76, 813
Sulentic J. W., Stirpe G. M., Marziani P., Zamanov R., Calvani M., Braito V., 2004, A&A, 423, 121
Taylor A. C., Grainge K., Jones M. E., Pooley G. G., Saunders R. D. E., Waldram E. M., 2001, MNRAS, 327, L1
Tielens A. G. G. M., Miley G. K., Willis A. G., 1979, A&AS, 35, 153
Tingay S. J., 2004, AJ, 127, 10
Waldram E. M., Pooley G. G., Grainge K. J. B., Jones M. E., Saunders R. D. E., Scott P. F., Taylor A. C., 2003, MNRAS, 342, 915
Waldram E. M., Pooley G. G., Davies M. L., Grainge K. J. B., Scott P. F., 2009, preprint (arXiv:0908.0066)
Wright E. L., Chen X., Odegard N. et al., 2009, ApJS, 180, 283

APPENDIX A: *WMAP* SOURCES MISSING FROM THE AT20G CATALOGUE

Table A1 lists the eight *WMAP* sources that do not have a catalogued bright (>250 mJy) AT20G source within 21.35 arcmin of the *WMAP* position. These 'missing' sources fall into several categories which are discussed in the following sections.

Table A1. The eight southern WMAP sources that are not matched with a bright (>250 mJy beam^{-1}) AT20G source within a matching radius of 21.35 arcmin. The listed WMAP K-band (23 GHz) flux densities are from the 5-year catalogue (Wright et al. 2009).

WMAP position (J2000)	WMAP S_{23} (Jy)	± (Jy)	AT20G S_{20} (Jy)	Notes
01 33 26.6−36 27 09	0.6	0.1	−	WMAP source is a hotspot of the radio galaxy NGC 612 (see the text)
03 22 25.4−37 11 25	18.5	3.1	−	Radio galaxy Fornax A (see the text)
05 19 21.6−05 39 37	2.4	0.1	−	Blend of Galactic emission nebulae (Wright et al. 2009), no AT20G counterpart
06 32 21.1−69 28 32	0.4	0.0	−	No AT20G counterpart
06 36 31.8−20 31 38	1.1	0.0	0.13	Part of the radio galaxy PKS 0634−20, matched with two faint AT20G sources
11 50 12.9−79 27 35	1.2	0.0	−	No AT20G counterpart
16 37 52.5−77 14 58	1.4	0.1	0.04	Faint AT20G counterpart (see the text)
22 29 47.1−20 50 28	0.9	0.1	−	Part of the Galactic planetary nebula NGC 7293, no AT20G counterpart

A1 Bright nearby radio galaxies with large angular size

As noted by Massardi et al. (2008), the radio galaxy Fornax A (*WMAP* J0322−3711) is not detected in the AT20G survey because most of its 20 GHz flux density arises from diffuse emission associated with the lobes, which are resolved out by the 2 arcmin ATCA beam. Fornax A is the only bright extragalactic source known to be missing from the AT20G catalogue.

Two other *WMAP* sources (J0133−3627 and J0636−2031) correspond to peaks in the extended emission of the nearby radio galaxies NGC 612 and PKS 0634−20, respectively. Both these galaxies are detected by AT20G, and the large *WMAP*–AT20G position offsets arise from the complex structure of the extended radio emission.

A2 Extended Galactic sources

Two *WMAP* objects (J0519−0539 and J2229−2050) are associated with extended Galactic sources. Wright et al. (2009) note that J0519−0539 is a blend of two Lynds Bright Nebulae, LBN 207.65−23.11 and LBN 207.29−22.66, while J0636−2031 is part of the Helix Nebula, NGC 7293. Both objects are significantly larger than the AT20G beam, and appear to be mostly resolved out in our survey.

A3 Extragalactic *WMAP* sources not found in AT20G

There are three remaining *WMAP* sources (J0632−6928, J1150−7927 and J1637−7714) for which no obvious counterpart can be found in the AT20G catalogue. All three of these sources are detected in each of the five *WMAP* single-year images (Wright et al. 2009), and do not appear to vary significantly in flux density over this 5-year time-span.

In two cases (*WMAP* J0632−6928 and J1150−7927), there is no catalogued AT20G source within the 0°.9 *WMAP* beam at the listed *WMAP* position. Unless these *WMAP* sources are very diffuse, it seems unlikely that they are real.

J0632−6928 has a *WMAP* flux density of 0.4 Jy, making it the weakest K-band (23 GHz) detection in the Wright et al. (2009) catalogue, but it is detected (as a sub-Jy source) in all five *WMAP* bands. The closest AT20G source, J063455−694532, is 0°.4 away and has a flux density of 66 mJy beam^{-1} at 20 GHz and 154 mJy beam^{-1} at 5 GHz. Its PMN counterpart is PMN J0634−6945 with a flux density of 92 ± 8 mJy beam^{-1}, and the SUMSS flux density is 123.1 ± 3.8 mJy beam^{-1}. AT20G J063455−694532 seems too faint to be a plausible identification for the *WMAP* source.

The third source (*WMAP* J1637−7714) is identified by Wright et al. (2009) with a nearby 5 GHz source PMN J1636−7713, which is also detected as a weak (40 ± 2 mJy beam^{-1} at 20 GHz) AT20G source. Once again, however, the catalogued AT20G flux density is well below the *WMAP* detection limit. A stronger AT20G source (AT20G J164416−771548, with a 20 GHz flux density of 399 ± 20 mJy beam^{-1}) lies 22 arcmin from the *WMAP* position, and may be responsible for the *WMAP* detection.

SUPPORTING INFORMATION

Additional Supporting Information may be found in the online version of this article:

Table 5. The AT20G source catalogue.

Please note: Wiley-Blackwell are not responsible for the content or functionality of any supporting materials supplied by the authors. Any queries (other than missing material) should be directed to the corresponding author for the article.

This paper has been typeset from a TEX/LATEX file prepared by the author.